AD-A052 155 TRW INC CLEVELAND OHIO MATERIALS TECHNOLOGY F/G 11/6
EFFECT OF RARE EARTH ADDITIONS ON STRESS CORROSION CRACKING OF --ETC(U)
JAN 78 A A SHEINKER N00014-74-C-0365
UNCLASSIFIED ER-7814-3 NL

| OF |
AD
A052155

END
DATE
FILMED
5-78
DDC

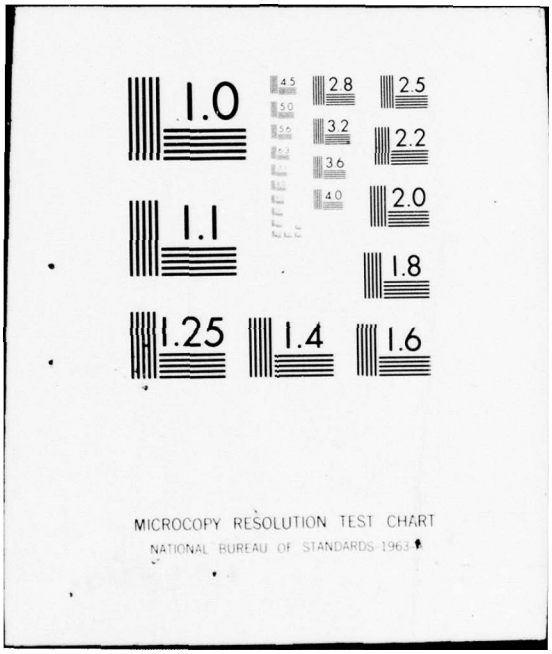
1.0
1.1
1.25
1.4
1.6
1.8
2.0
2.2
2.5
2.8
3.2
3.6
4.0
4.5
5.0
5.6
MICROCOPY RESOLUTION TEST CHART
NATIONAL BUREAU OF STANDARDS-1963-A

ER-7814-3

14

B.S.

EFFECT OF RARE EARTH ADDITIONS ON STRESS CORROSION CRACKING OF 4340 STEEL

By

A. A. SHEINKER

TECHNICAL REPORT

Prepared for

Office of Naval Research

Contract N00014-74-C-0365

JANUARY 1978

TRW

EQUIPMENT
MATERIALS TECHNOLOGY

ER 7814-3

TECHNICAL REPORT

EFFECT OF RARE EARTH ADDITIONS ON STRESS CORROSION CRACKING OF 4340 STEEL

Prepared for

Office of Naval Research
Contract N00014-74-C-0365

January 1978

by
A. A. Sheinker

TRW Inc.
TRW Equipment
Materials Technology
Cleveland, Ohio 44117

FOREWORD

The work described in this report was performed in the Materials Technology Laboratory of TRW Inc., under the sponsorship of the Office of Naval Research, Contract N00014-74-C-0365. Dr. P. A. Clarkin acted as Program Monitor for the Navy. The program was administered for TRW by Dr. C. S. Kortovich, Program Manager. The Principal Investigator was Dr. A. A. Sheinker, with technical assistance provided by Mr. J. W. Sweeney and Mr. R. R. Ebert. Work conducted during the first two years of this contract involved a study of the effect of rare earth additions on the hydrogen embrittlement resistance of cathodically charged and cadmium plated 4340 steel. Work conducted during the third year, covered in this report, consisted of a study of the effect of rare earth additions on the stress corrosion cracking resistance of 4340 steel in salt water.

This report has been assigned TRW Equipment Number ER 7814-3 and the data are recorded in laboratory notebook Number 794.

ABSTRACT

The addition of rare earth elements was investigated as a method of improving the stress corrosion cracking resistance of high strength steels. The addition of cerium at levels of 0.20 and 0.30 weight percent had only a small effect on the stress corrosion cracking resistance of AISI 4340 steel heat treated to a yield strength of approximately 215 ksi (1480 MPa). The stress corrosion cracking threshold (K_{Iscc}) in 3.5 percent sodium chloride solution at room temperature was about the same for the two cerium-bearing steels as it was for 4340 steel without cerium, ranging from 15 to 17 ksi $\sqrt{in.}$ (16.5 to 19 MPa $\sqrt{m}$). The higher cerium (0.30%) material had longer failure times and lower average crack growth rates than the lower cerium (0.20%) material. The failure times and average crack growth rates for the steel without cerium could not be directly compared with those for the two cerium-bearing steels because of crack branching, which occurred only in the material without cerium. However, it was estimated that, in the absence of branching, the failure times for the non-cerium steel would be shorter and the average crack growth rates higher than those for the lower cerium steel. The cerium additions had no effect on the fractographic morphology of stress corrosion cracking, which was intergranular at low stress intensity levels, with an increasing proportion of dimpled rupture as the stress intensity level increased.

TABLE OF CONTENTS

I INTRODUCTION

High strength steels, particularly the low alloy martensitic types, are susceptible to stress corrosion cracking in a wide variety of both aqueous and nonaqueous environments (1-4). For a given type of steel, the resistance to stress corrosion cracking decreases with increasing yield strength (1-4). Thus, for applications in which the metal is exposed to a hostile environment, the high load-bearing capabilities of these materials cannot be fully exploited because of the increased possibility of service failures due to stress corrrosion cracking.

Considerable research in the past decade has led to the conclusion that stress corrosion cracking in most high strength steels is a form of hydrogen embrittlement (3, 5, 6). The hydrogen-bearing environment present in a crack reacts with the metal at the tip of the crack to form hydrogen, which enters the triaxially stressed metal at the crack tip and results in local embrittlement and crack growth. Therefore, there is a strong relationship between the stress corrosion cracking resistance of a high strength steel and its hydrogen embrittlement resistance.

There are two forms of hydrogen embrittlement phenomena: (1) internal hydrogen embrittlement, which is associated with the presence of hydrogen in the metal due to prior processing, and (2) environmental hydrogen embrittlement, which results from the entry of hydrogen into the metal during exposure to a hydrogen-bearing service environment, as in stress corrosion cracking. It is generally accepted that the mechanism of embrittlement is the same in both forms, but that the processes of hydrogen transport are different. The essential difference between internal and environmental hydrogen embrittlement is the source of hydrogen, resulting in different hydrogen transport processes for the two forms of embrittlement. In the internal form, hydrogen is already present in the metal when it is placed into service and diffuses through the bulk metal to cause embrittlement. In the environmental form, hydrogen must enter the metal from the service environment, so that metal-environment reactions at the metal surface play an important role and hydrogen diffusion occurs over only a short distance below the surface or near a crack tip.

The current methods of inhibiting hydrogen embrittlement in high strength steels include changes in microstructure, changes in alloy composition, baking, surface prestressing, plating, cathodic protection, nonmetallic coating, selective changes in surface composition by heat treatment and modification of the embrittling environment. All of these methods have serious limitations in practical applications so that no truly satisfactory method of inhibiting hydrogen embrittlement has been found. However, a new method which has considerable potential is the addition of rare earth elements to high strength steels. In previous work under this contract (7), it was shown that the addition of either 0.17 weight percent cerium or 0.16 weight percent lanthanum substantially improved the internal hydrogen embrittlement resistance of AISI 4340 steel at a yield strength level of approximately 205 ksi. This improvement was manifested in hydrogen-charged specimens by (1) longer crack growth incubation times, (2) lower crack growth rates, (3) longer failure times, and (4) higher threshold stress intensities, as compared with non-rare earth treated 4340 steel. The most significant aspects of this increased resistance to internal hydrogen embrittlement were associated

with the lower crack growth rates and the higher threshold stress intensities. The crack growth rates for the rare earth materials were about an order of magnitude lower than those for the non-rare earth 4340 steel. The threshold stress intensities (i.e., the stress intensity levels below which failure did not occur) of the rare earth materials were approximately four times higher than that of the non-rare earth 4340 steel. The purpose of the present study was, therefore, to extend this concept to stress corrosion cracking to determine whether rare earth additions can increase the stress corrosion cracking resistance of high strength steels.

II EXPERIMENTAL PROCEDURE

The test material was obtained by making three experimental 50-pound (23-kg) heats of 4340 steel containing zero, 0.20, and 0.30 weight percent cerium. The chemical compositions of the three heats are presented in Table 1, along with the specified composition ranges for AISI 4340 steel. All of the standard elements were within the specified ranges, except the silicon and molybdenum in heat X792, which were slightly higher. However, silicon and molybdenum at these levels have a negligible effect on stress corrosion cracking in 4340 steel (4,8,9). The presence of small amounts of lanthanum in the two cerium-bearing heats was due to the presence of lanthanum in the cerium silicide used for making the cerium additions.

The three heats were vacuum-induction melted and aluminum deoxidized and the cerium was added after deoxidation. The heats were cast in the form of tapered round ingots measuring 4 inches (0.10 m) in diameter at the bottom, 4-3/4 inches (0.12 m) in diameter at the top, and 10 inches (0.25 m) tall. The three ingots were forged in four passes at 2150°F (1450°K), cross-rolled in two passes at 1950°F (1340°K), and straight-rolled in two passes at 1950°F (1340°K) to obtain three plates, 3/4 inch (0.019m) thick by 8-1/2 inches (0.22 m) wide by 20 inches (0.51 m) long. The plates were then annealed at 1150°F (894°K) for 8 hours. This ingot breakdown procedure demonstrated the workability of 4340 steel made with the levels of rare earth additions studied in this program.

Prior to finish machining, the test specimens cut from the three plates were heat treated as follows:

1. Normalized at 1700°F (1200°K) for 15 minutes in salt bath and air cooled.
2. Austenitized at 1550°F (1120°K) for 30 minutes in salt bath and oil quenched.
3. Tempered at 450°F (505°K) for 1 hour plus 1 hour in air, and air cooled.

The 450°F (505°K) tempering temperature was chosen to obtain a high strength level and thus increased susceptibility to stress corrosion cracking in this steel (4,10).

The conventional mechanical properties of the three heats were evaluated by performing duplicate tensile and Charpy impact tests at room temperature on both longitudinal and transverse specimens. The dimensions of the test specimens are shown in Figure 1. The hardness of the heat treated specimens was Rockwell C51.

Stress corrosion cracking tests were conducted at room temperature on the precracked compact tension specimens shown in Figure 2. These specimens were machined from the plates in the T-L orientation, i.e., with the direction normal to the crack plane (loading direction) parallel to the width direction of the plate and the direction of expected crack propagation coincident with the longitudinal direction of the plate. The saw-cut notch was extended 0.050 inch (0.0013 m) by electrical discharge machining (EDM) in order to promote fatigue crack initiation. The specimens were precracked by cyclic tension-tension loading on a Sonntag SF-4 fatigue testing machine at a frequency of 60 hz and a load ratio (R = ratio of minimum load to maximum load) of 0.200. The fatigue cracks were grown to a length of 0.15 inch (0.0038 m) beyond the EDM slot to obtain a total precrack length of 0.58 inch (0.015 m)

Table I

Compositions of 4340 Steel Heats, Weight Percent

Element	AISI 4340 Specification	Heat X794	Heat X793	Heat X792
C	0.38-0.43	0.41	0.41	0.40
Mn	0.60-0.80	0.73	0.71	0.72
P	0.040 Max.	0.008	0.008	0.008
S	0.040 Max.	0.005	0.003	0.003
Si	0.20-0.35	0.28	0.30	0.45
Ni	1.65-2.00	1.77	1.74	1.72
Cr	0.70-0.90	0.80	0.71	0.71
Mo	0.20-0.30	0.28	0.30	0.32
Al	-	0.043	0.064	0.070
Ce	-	0	0.20	0.30
La	-	0	0.019	0.023

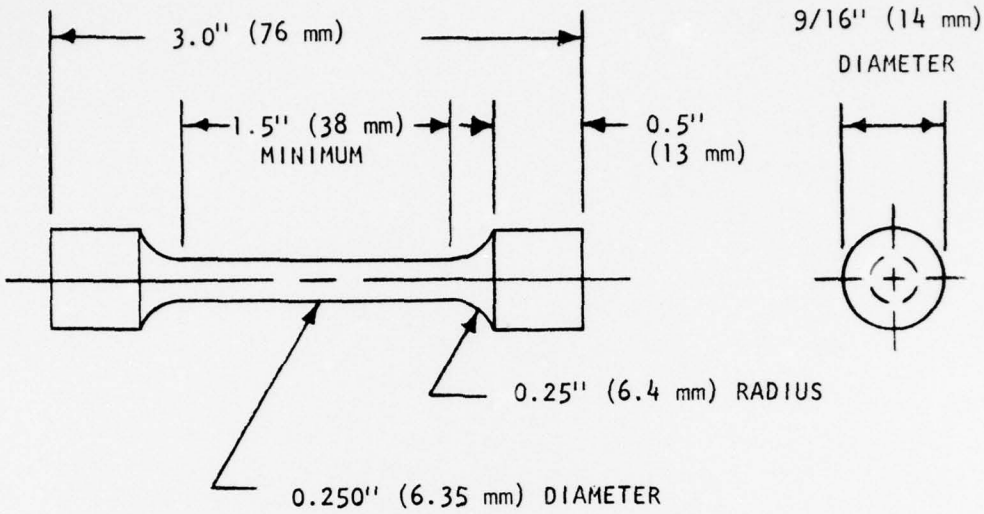

(a) Tensile test specimen.

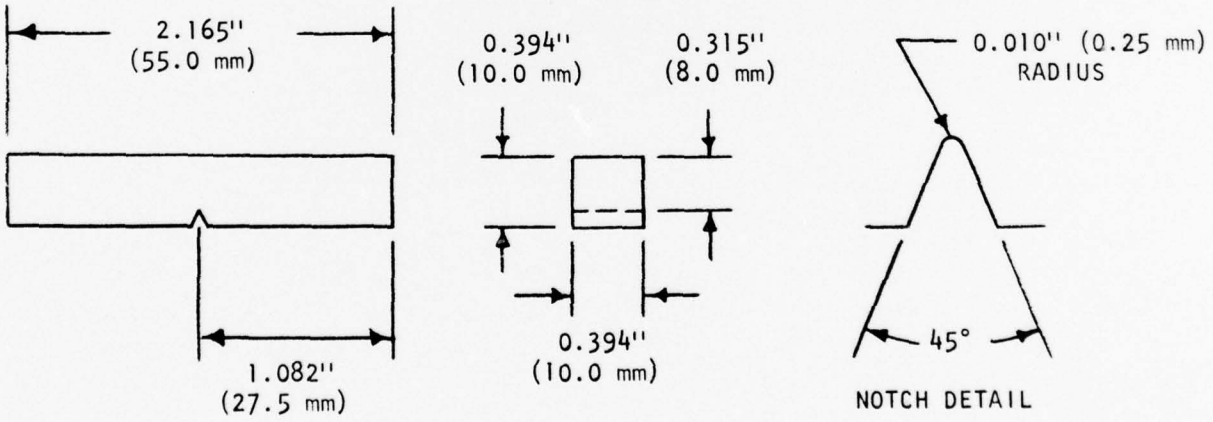

(b) Charpy impact test specimen.

Figure 1. Tensile and Charpy impact test specimens used in mechanical property characterization.

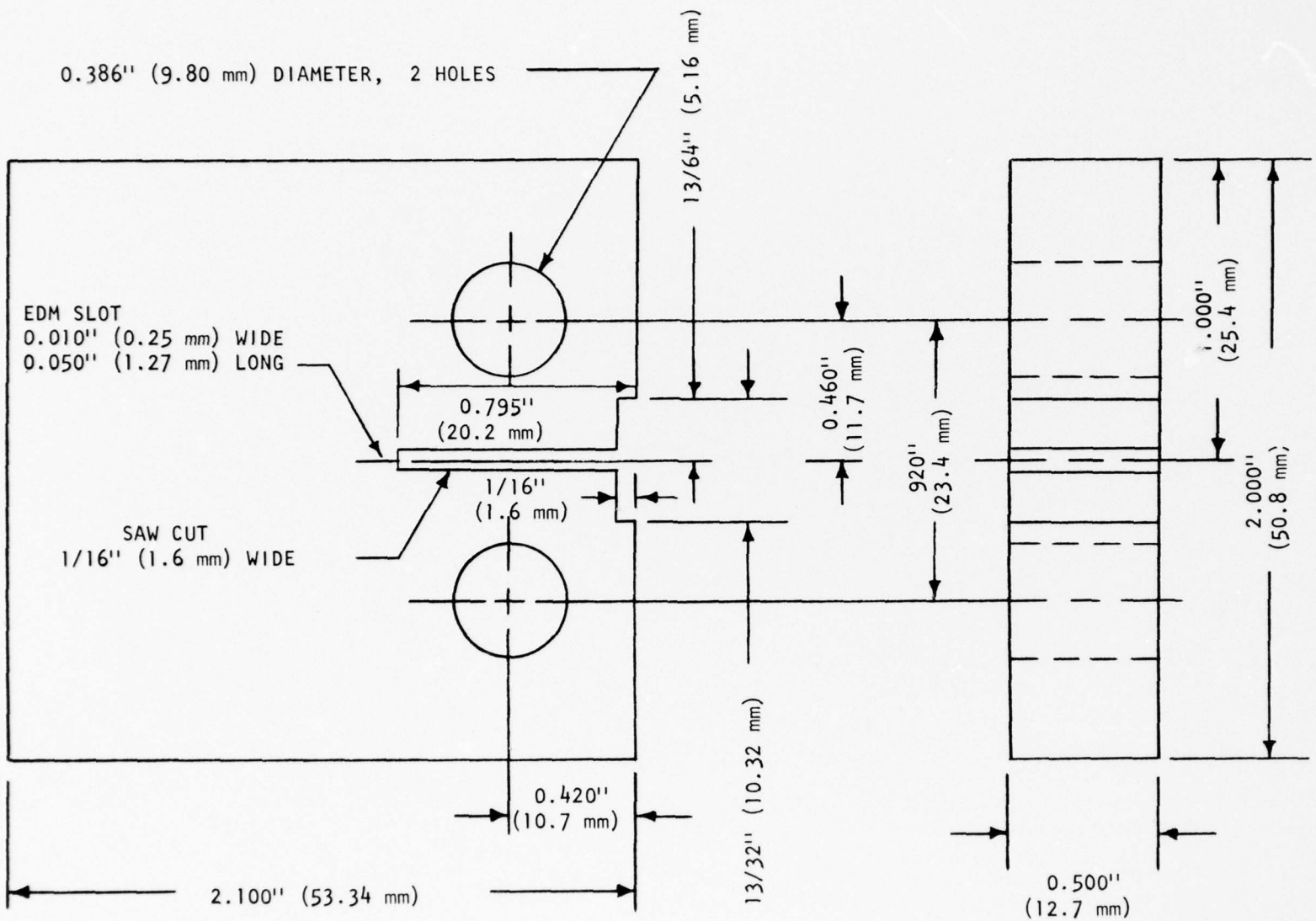

Figure 2. Precracked compact tension specimen used in stress corrosion cracking tests.

measured from the load line. The fatigue cracks were produced in 25,000 to 50,000 cycles and the maximum stress intensity factor (K_I) at the conclusion of precracking was 23 ksi $\sqrt{in.}$ (25 MPa $\sqrt{m}$). All of the fatigue cracks grew straight and perpendicular to the loading direction.

The stress corrosion cracking tests were conducted under sustained load on Satec self-leveling, lever-loaded creep rupture testing machines. The test environment was an aqueous solution of 3.5 percent sodium chloride, which is commonly employed in stress corrosion studies. The compact tension specimens were completely immersed in the test environment by surrounding the specimen with a plexiglass container fastened to the lower pull rod and filling the container with the corrodent. The specimens were immersed in the corrodent prior to application of the load in order to promote immediate wetting of the precrack tip. Tests were conducted at various initial stress intensity (K_{Ii}) levels to determine failure time as a function of K_{Ii} and the stress corrosion cracking threshold (K_{Iscc}, the stress intensity level below which failure is not observed) for each heat of steel. Stress intensity factors were calculated from the equation (11)

$$K_I = \frac{P}{B\sqrt{W}} \left[29.6 \left(\frac{a}{W}\right)^{1/2} - 185.5 \left(\frac{a}{W}\right)^{3/2} + 655.7 \left(\frac{a}{W}\right)^{5/2} \right.$$
$$\left. -1017 \left(\frac{a}{W}\right)^{7/2} + 638.9 \left(\frac{a}{W}\right)^{9/2} \right]$$

where P = applied load, pounds (newtons)

B = specimen thickness, inches (meters)

W = specimen width measured from load line, inches (meters)

a = crack length measured from load line, inches (meters).

The tests were terminated after 10,000 minutes if failure did not occur sooner. A total of 17 stress corrosion cracking tests were performed for each heat of steel. The fracture surfaces of selected failed specimens were examined in the scanning electron microscope to determine the morphology of crack propagation.

III RESULTS AND DISCUSSION

A. Mechanical Property Characterization

The mechanical properties of the three heats of 4340 steel are presented in Table 2 and plotted as a function of cerium content in Figures 3, 4, and 5. Following the same trends as in the previous study (7), the strength, ductility and impact resistance all decreased with increasing cerium content. These reductions were attributed to the presence of continuous networks of rare earth oxide inclusions at the prior austenite grain boundaries, as shown in Figure 6. There were no significant differences between the longitudinal and transverse mechanical properties of any of the three steels, probably because the plates had been cross-rolled.

The decreases in strength with increasing cerium content were small. The greatest reduction in average yield strength was only 2.1 percent for the 0.20% Ce steel in the transverse direction, while the greatest reduction in average ultimate tensile strength was only 3.8 percent for the 0.30% Ce steel in the transverse direction. However, the decreases in ductility and impact resistance were substantial, particularly at the 0.30% Ce level. For example, the average longitudinal elongation decreased 20 percent at the 0.20% Ce level and 65 percent at the 0.30% Ce level, and the average longitudinal reduction of area decreased 30 percent at the 0.20% Ce level and 82 percent at the 0.30% Ce level. The average Charpy impact energy in the longitudinal direction decreased 45 percent at the 0.20% Ce level and 60 percent at the 0.30% Ce level.

The 0.20% Ce steel met the current ductility requirements for aircraft quality 4340 steel in this temper condition (6% minimum transverse elongation, and 25% minimum and 30% average transverse reduction of area) (12), whereas the 0.30% Ce steel did not. However, it is recognized that these cerium levels are higher than the levels of rare earth additions currently used in steelmaking technology and were employed to study the effect of high rare earth levels on stress corrosion cracking susceptibility.

B. Stress Corrosion Cracking Results

The stress corrosion test results for the three heats of 4340 steel are presented in Tables 3, 4, and 5. Failure times are plotted as a function of initial stress intensity (K_{Ii}) in Figures 7, 8, and 9, and the three time-to-failure versus K_{Ii} curves are shown for comparison in Figure 10. Average crack growth rates (da/dt) are plotted as a function of K_{Ii} in Figures 11, 12, and 13, and the three da/dt versus K_{Ii} curves are shown for comparison in Figure 14. The average crack growth rate for each specimen was determined by measuring the length of the stress corrosion crack (from the end of the fatigue precrack to the onset of rapid fracture) observed on the fracture surface and dividing this length by the failure time.

Table 2

Mechanical Properties of 4340 Steel Heats

Heat No.	Cerium Content, %	Orientation	Yield Strength at 0.2% Offset ksi	Yield Strength at 0.2% Offset MPa	Ultimate Tensile Strength ksi	Ultimate Tensile Strength MPa	Elongation, %	Reduction of Area, %	Charpy Impact Energy ft-lb	Charpy Impact Energy J
X794	0	Longit.	216	1490	267	1840	14.5	51.6	21.0	28.5
		Longit.	215	1480	266	1830	13.0	51.0	20.5	27.8
		Transverse	219	1510	265	1830	14.0	50.8	20.0	27.1
		Transverse	216	1490	267	1840	14.0	51.0	21.5	29.2
X793	0.20	Longit.	212	1460	261	1800	10.0	32.8	9.5	12.9
		Longit.	213	1470	259	1790	12.0	38.9	13.5	18.3
		Transverse	212	1460	261	1800	12.0	35.6	11.5	15.6
		Transverse	214	1480	262	1810	11.0	32.1	10.5	14.2
X792	0.30	Longit.	216	1490	263	1810	6.0	10.5	8.0	10.8
		Longit.	210	1450	259	1790	3.5	7.8	8.5	11.5
		Transverse	217	1500	258	1780	5.0	6.3	9.0	12.2
		Transverse	216	1490	254	1750	3.0	4.7	8.5	11.5

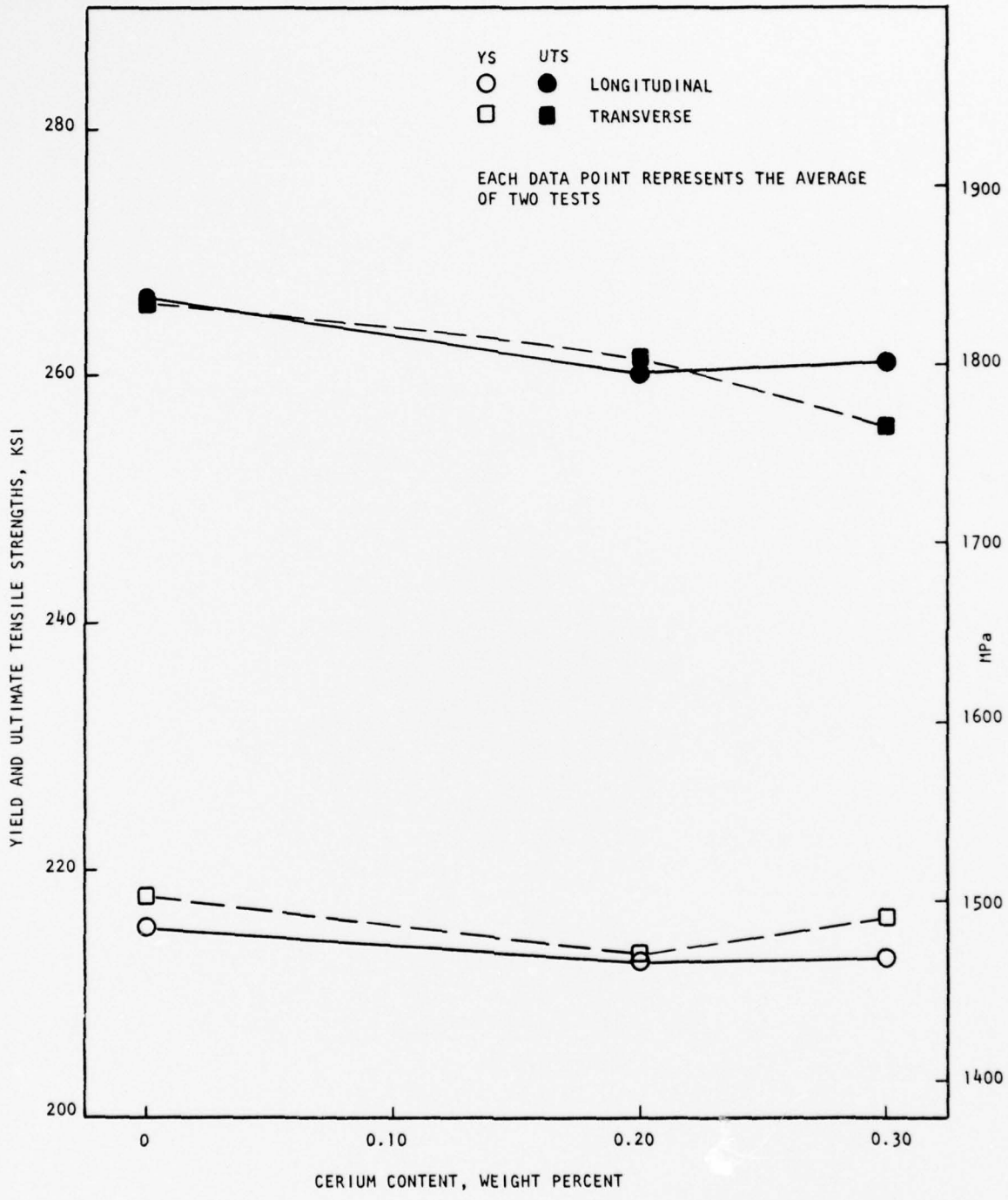

Figure 3. Yield and ultimate tensile strengths of 4340 steel as a function of cerium content.

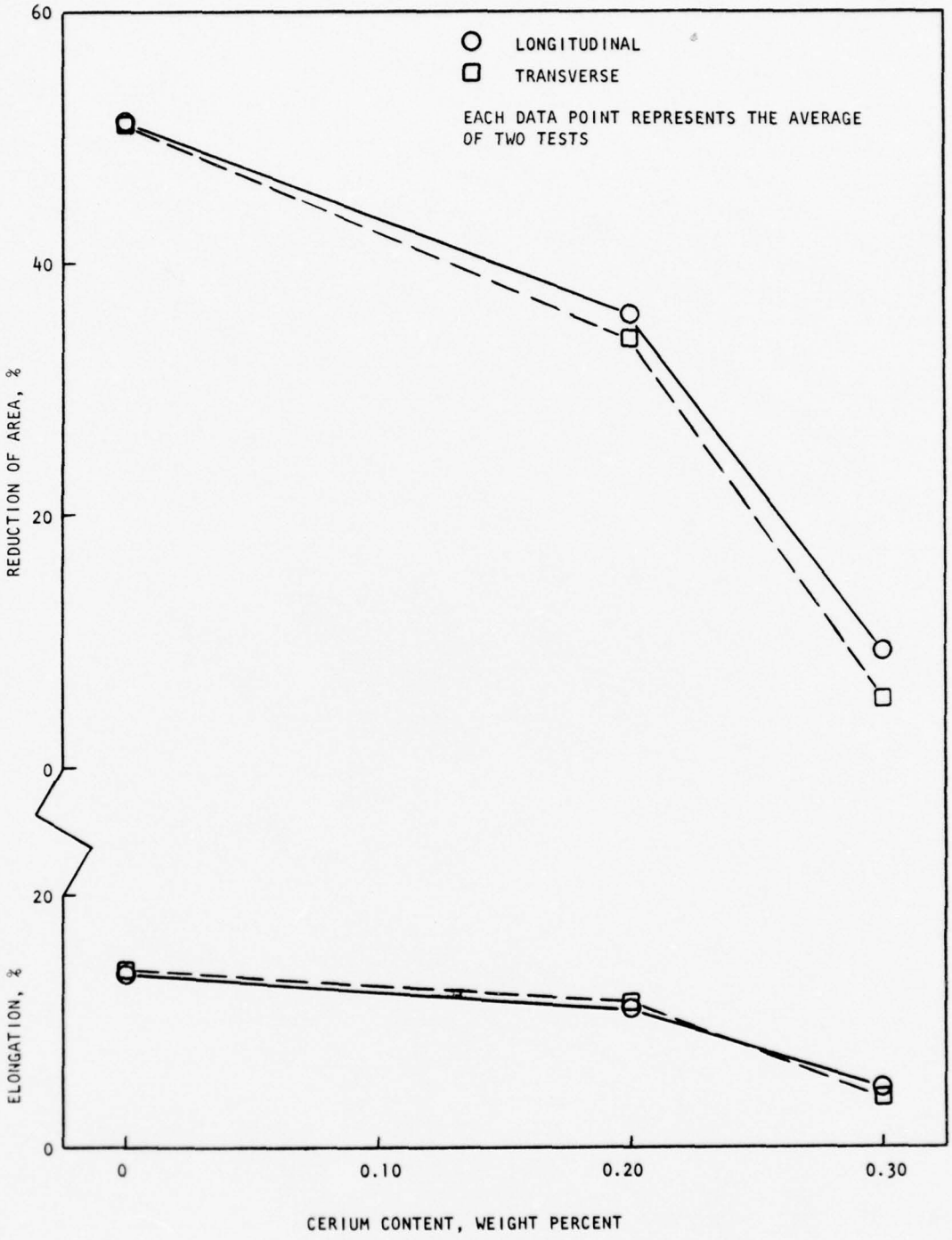

Figure 4. Elongation and reduction of area of 4340 steel as a function of cerium content.

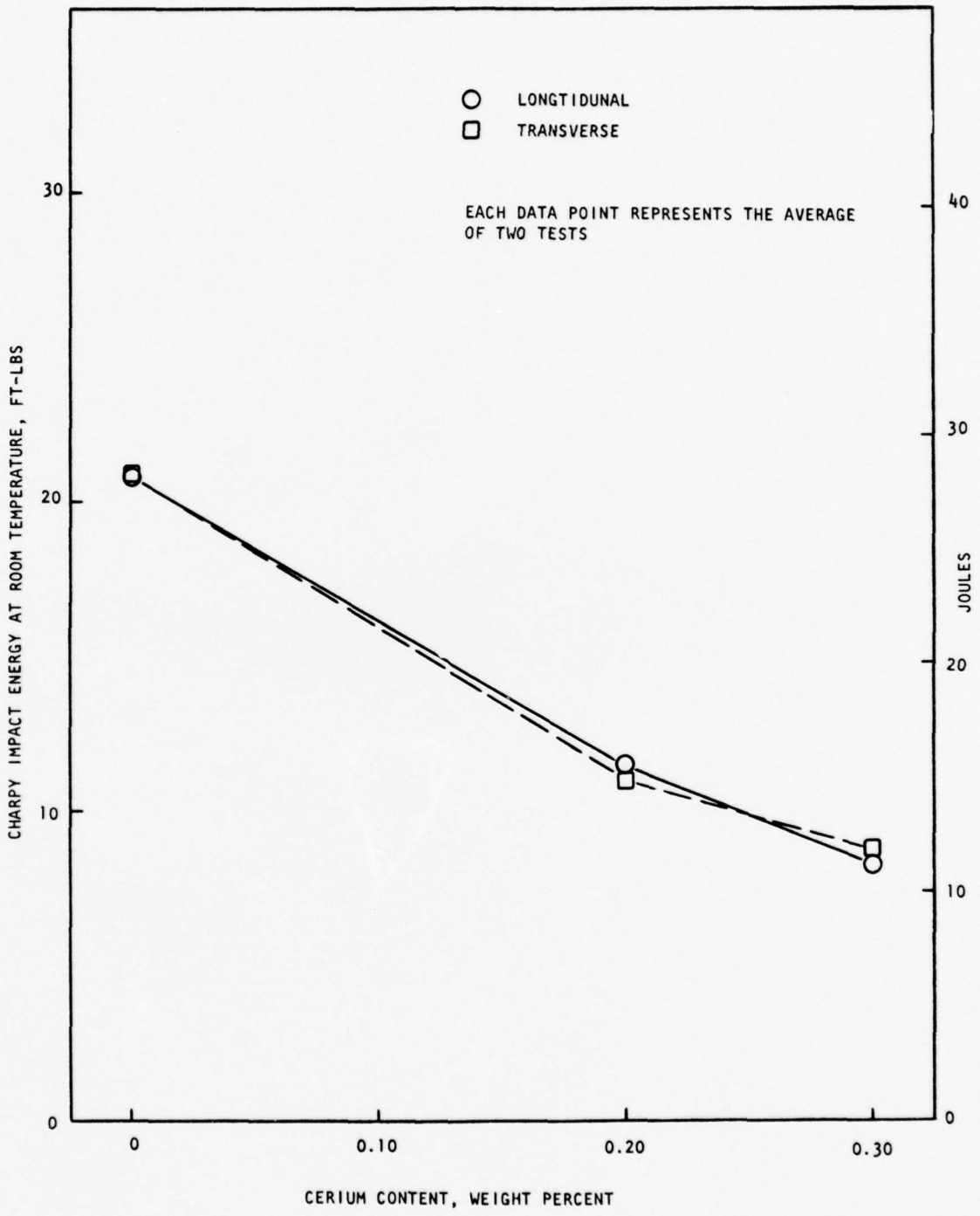

Figure 5. Charpy impact energy of 4340 steel as a function of cerium content.

Magnification, 125X

Magnification, 400X

Figure 6. Rare earth oxide inclusions at the prior austenite grain boundaries in plate from 4340 steel heat X792 (0.30% Ce) after heat treatment. Plane of plate is horizontal.

Table 3

Stress Corrosion Test Results for 4340 Steel Heat X794 (0% Ce)

Specimen Number	Initial Stress Intensity (K_{Ii}) ksi $\sqrt{in.}$	Initial Stress Intensity (K_{Ii}) MPa $\sqrt{m}$	Failure Time, Minutes	Average Crack Growth Rate (da/dt) in./minute	Average Crack Growth Rate (da/dt) M/S
2	14.1	15.5	(no failure)	0	0
10	15.7	17.2	1320	6.4×10^{-4}	2.7×10^{-7}
9	16.1	17.7	840	1.0×10^{-3}	4.4×10^{-7}
7	16.6	18.3	7824	1.0×10^{-4}	4.3×10^{-8}
3	17.1	18.8	(no failure)	0	0
6	17.1	18.8	918	9.5×10^{-4}	4.0×10^{-7}
8	17.2	18.9	990	8.1×10^{-4}	3.4×10^{-7}
4	17.4	19.2	4290	1.8×10^{-4}	7.7×10^{-8}
5	17.9	19.7	1446	5.5×10^{-4}	2.3×10^{-7}
1	18.8	20.6	588	1.4×10^{-3}	6.0×10^{-7}
11	27.8	30.5	450	1.6×10^{-3}	6.8×10^{-7}
12	36.9	40.5	438	1.6×10^{-3}	6.8×10^{-7}
13	46.7	51.3	444	1.4×10^{-3}	5.9×10^{-7}
14	57.2	62.9	312	1.5×10^{-3}	6.4×10^{-7}
15	64.8	71.2	318	1.5×10^{-3}	6.3×10^{-7}
16	75.2	82.6	222	1.7×10^{-3}	7.2×10^{-7}
17	85.9	94.4	0	-	-

Table 4

Stress Corrosion Test Results for 4340 Steel Heat X793 (0.20% Ce)

Specimen Number	Initial Stress Intensity (K_{Ii}) ksi $\sqrt{in.}$	Initial Stress Intensity (K_{Ii}) MPa $\sqrt{m}$	Failure Time, Minutes	Average Crack Growth Rate (da/dt) in./minute	Average Crack Growth Rate (da/dt) M/S
2	14.1	15.5	(No failure)	0	0
10	14.8	16.2	(No failure)	0	0
9	14.9	16.4	912	8.4×10^{-4}	3.6×10^{-7}
8	15.8	17.3	1878	4.0×10^{-4}	1.7×10^{-7}
3	16.9	18.5	(No failure)	0	0
7	17.0	18.7	1410	5.3×10^{-4}	2.3×10^{-7}
5	17.4	19.2	852	9.4×10^{-4}	4.0×10^{-7}
6	17.7	19.4	612	1.2×10^{-3}	5.2×10^{-7}
4	18.1	19.9	5304	1.4×10^{-4}	6.0×10^{-8}
1	18.8	20.7	468	1.5×10^{-3}	6.5×10^{-7}
11	28.3	31.0	204	2.8×10^{-3}	1.2×10^{-6}
12	38.0	41.8	156	2.6×10^{-3}	1.1×10^{-6}
13	41.8	46.0	108	3.7×10^{-3}	1.6×10^{-6}
14	46.4	51.0	90	4.4×10^{-3}	1.9×10^{-6}
15	52.1	57.2	66	5.3×10^{-3}	2.2×10^{-6}
16	57.1	62.8	54	-	-
17	60.8	66.8	30	-	-

Table 5

Stress Corrosion Test Results for 4340 Steel Heat X792 (0.30% Ce)

Specimen Number	Initial Stress Intensity (K_{Ii}) ksi $\sqrt{in.}$	Initial Stress Intensity (K_{Ii}) MPa $\sqrt{m}$	Failure Time, Minutes	Average Crack Growth Rate (da/dt) in./minute	Average Crack Growth Rate (da/dt) M/S
2	14.1	15.5	(No failure)	0	0
8	14.9	16.4	(No failure)	0	0
7	15.0	16.4	2598	2.9×10^{-4}	1.2×10^{-7}
6	15.4	16.9	3918	1.5×10^{-4}	6.2×10^{-8}
4	15.9	17.5	4554	1.6×10^{-4}	7.0×10^{-8}
3	17.1	18.8	3360	2.2×10^{-4}	9.4×10^{-8}
5	18.1	19.9	2070	3.4×10^{-4}	1.4×10^{-7}
1	19.2	21.1	1266	5.1×10^{-4}	2.2×10^{-7}
9	27.8	30.5	570	1.1×10^{-3}	4.8×10^{-7}
10	38.3	42.1	414	-	-
11	46.5	51.1	288	1.9×10^{-3}	8.1×10^{-7}
12	55.4	60.9	276	1.4×10^{-3}	6.1×10^{-7}
13	65.7	72.1	138	2.2×10^{-3}	9.2×10^{-7}
14	69.6	76.5	162	1.2×10^{-3}	5.2×10^{-7}
15	75.1	82.5	42	3.6×10^{-3}	1.5×10^{-6}
16	80.7	88.7	66	3.8×10^{-3}	1.6×10^{-6}
17	86.1	94.6	6	1.7×10^{-2}	7.1×10^{-6}

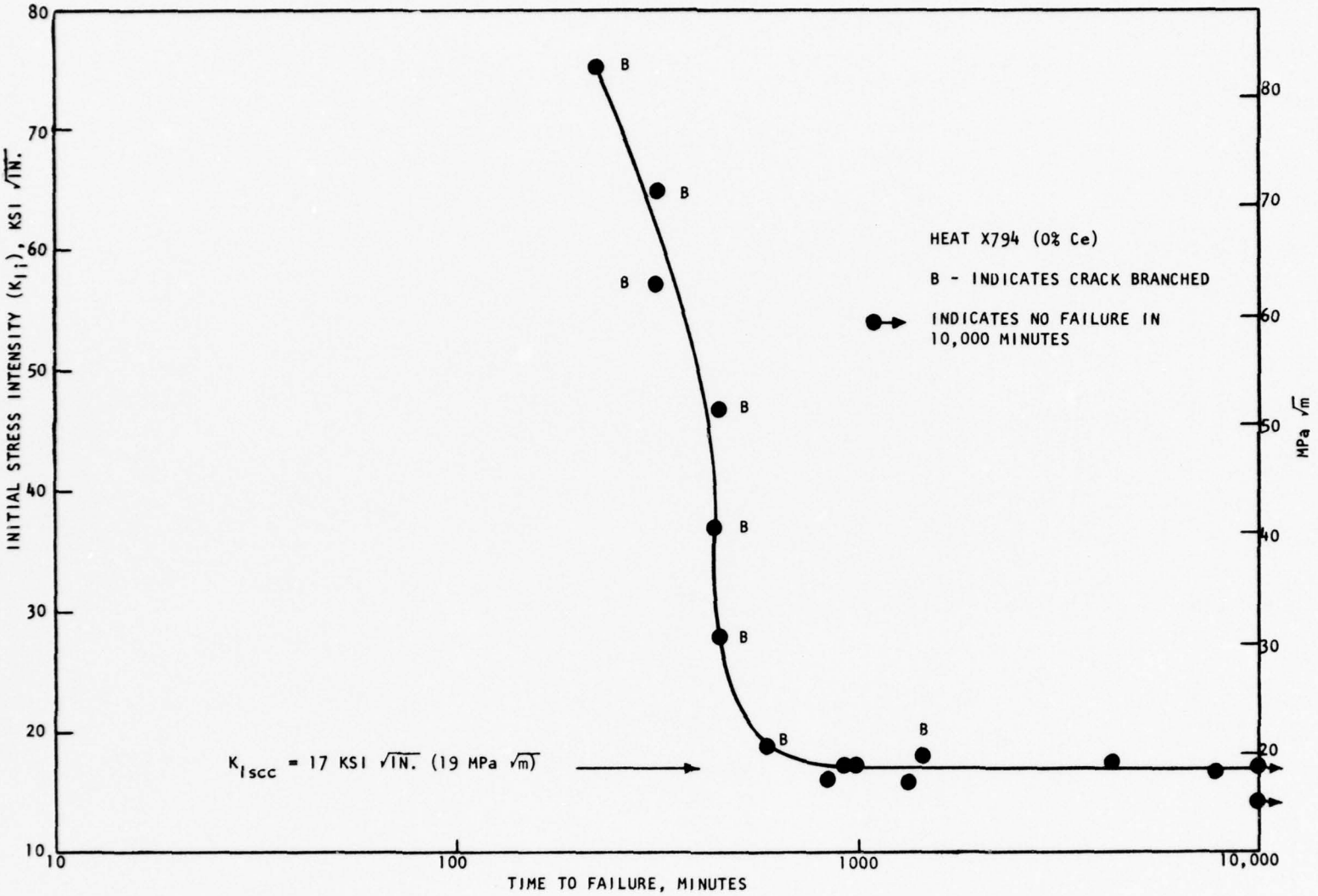

Figure 7. Stress corrosion failure time as a function of initial stress intensity for 4340 steel heat X794 containing no cerium.

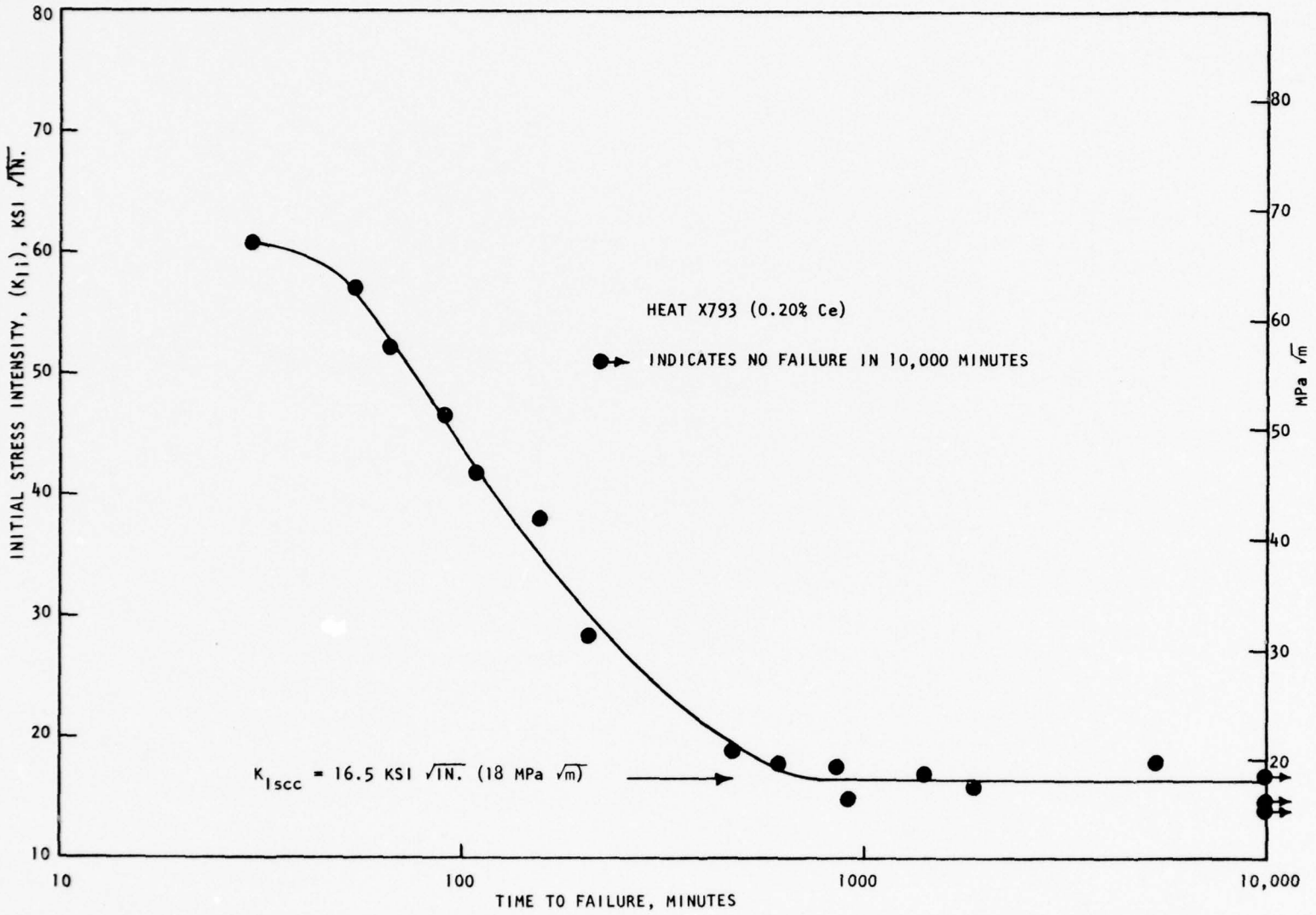

Figure 8. Stress corrosion failure time as a function of initial stress intensity for 4340 steel heat X793 containing 0.20% cerium

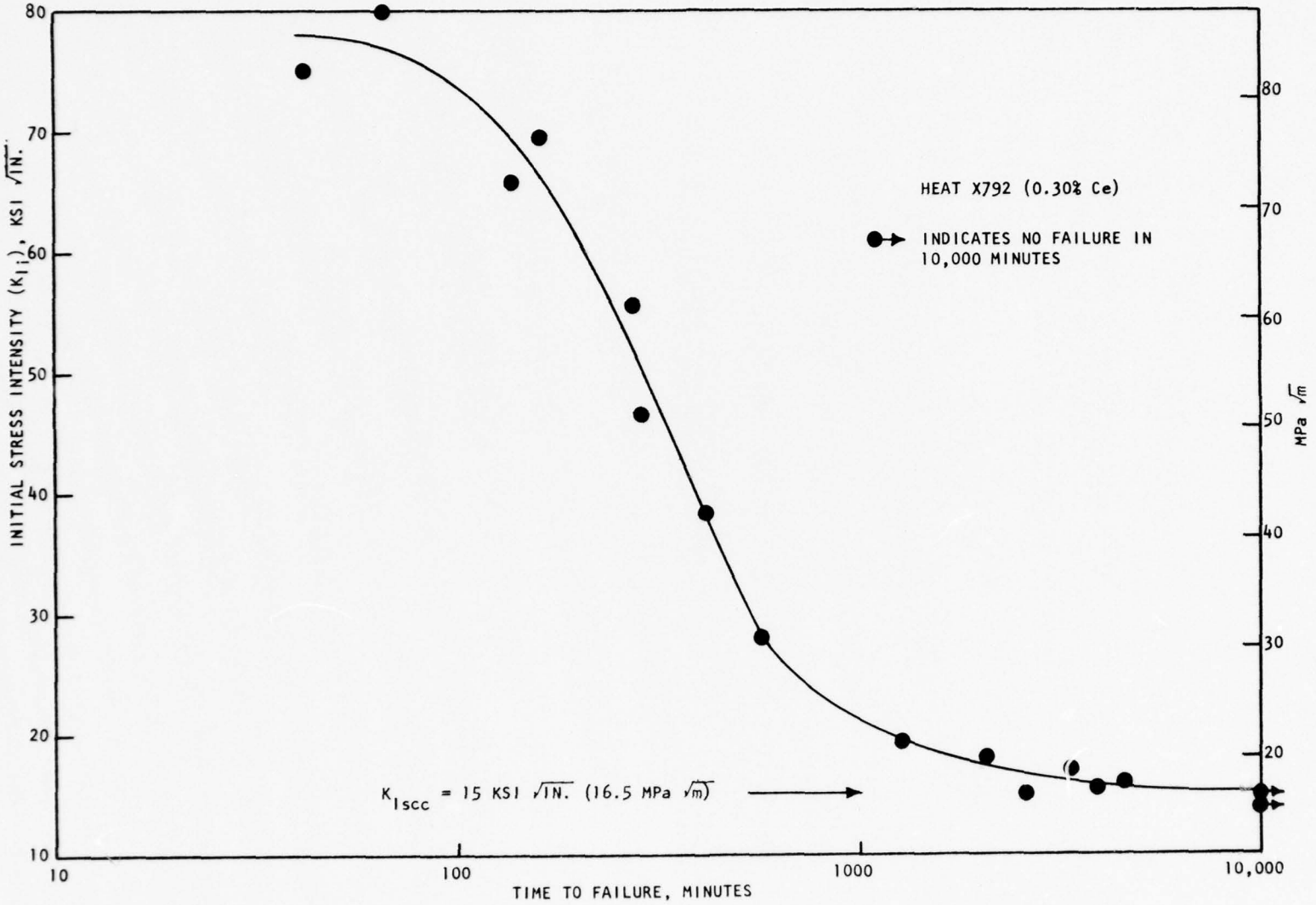

Figure 9. Stress corrosion failure time as a function of initial stress intensity for 4340 steel heat X792 containing 0.30% cerium.

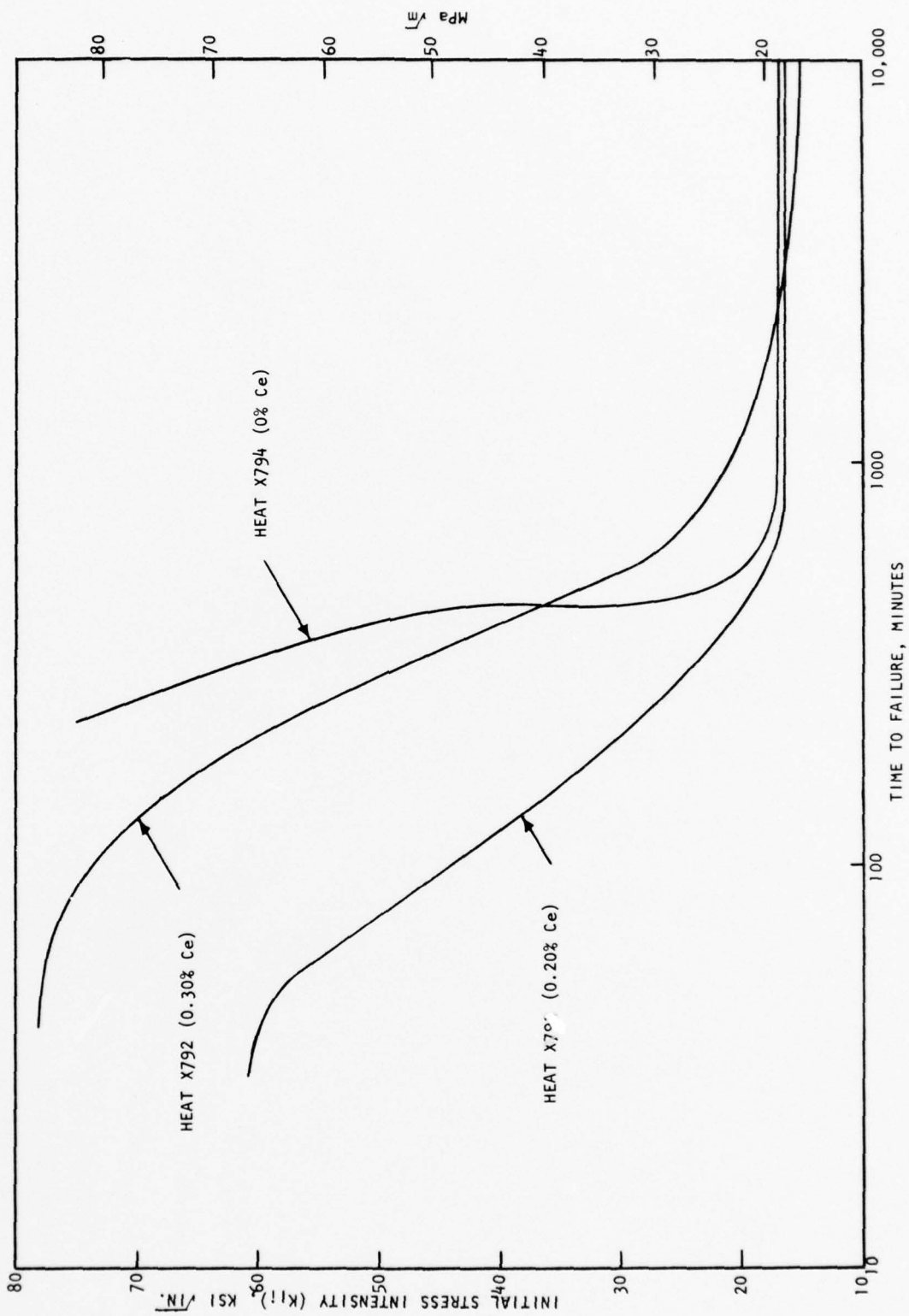

Figure 10. Comparison of stress corrosion failure time versus K_{1i} curves for 4340 steel with various cerium contents.

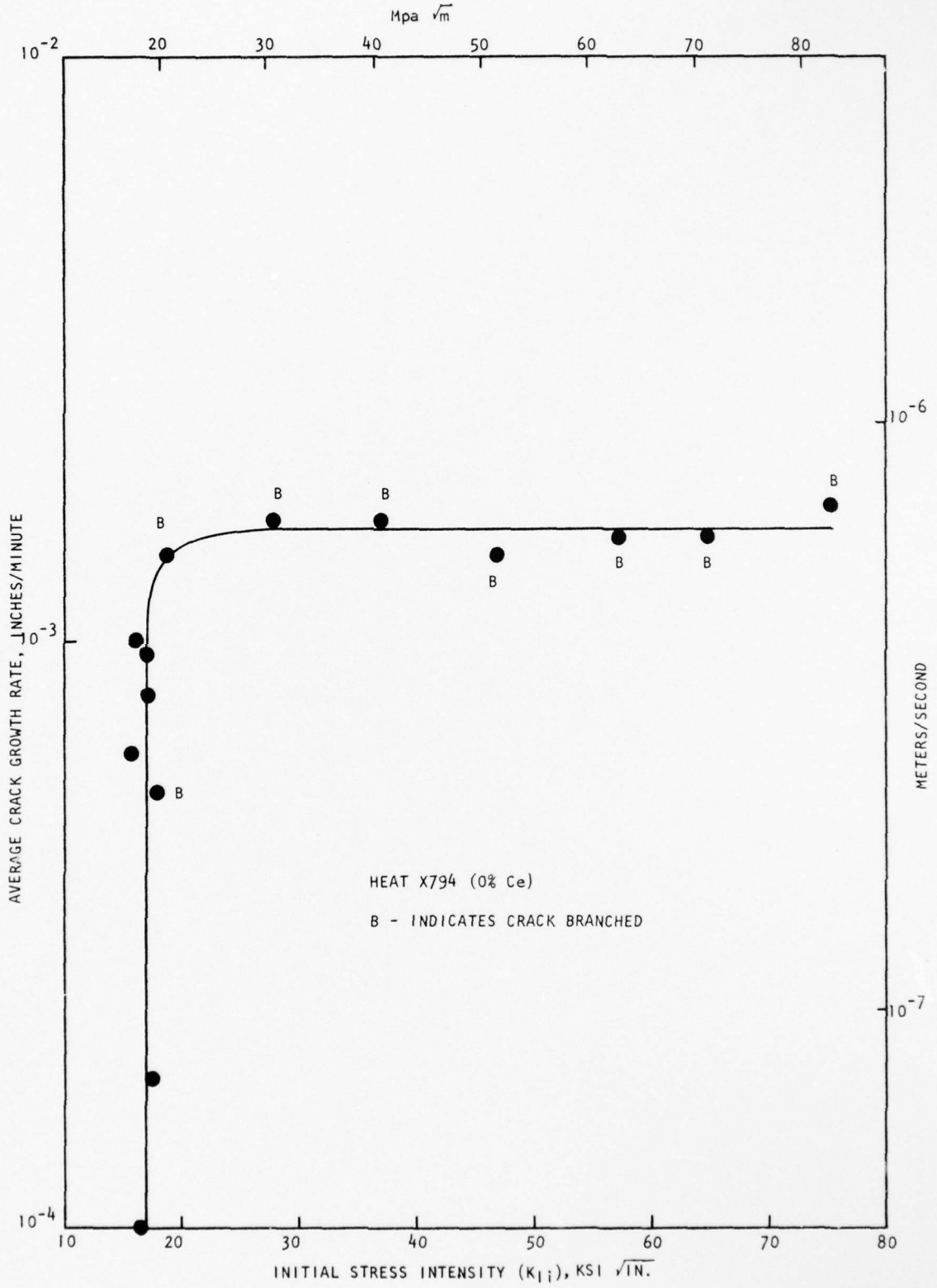

Figure 11. Stress corrosion crack growth rate as a function of initial stress intensity for 4340 steel heat X794 containing no cerium.

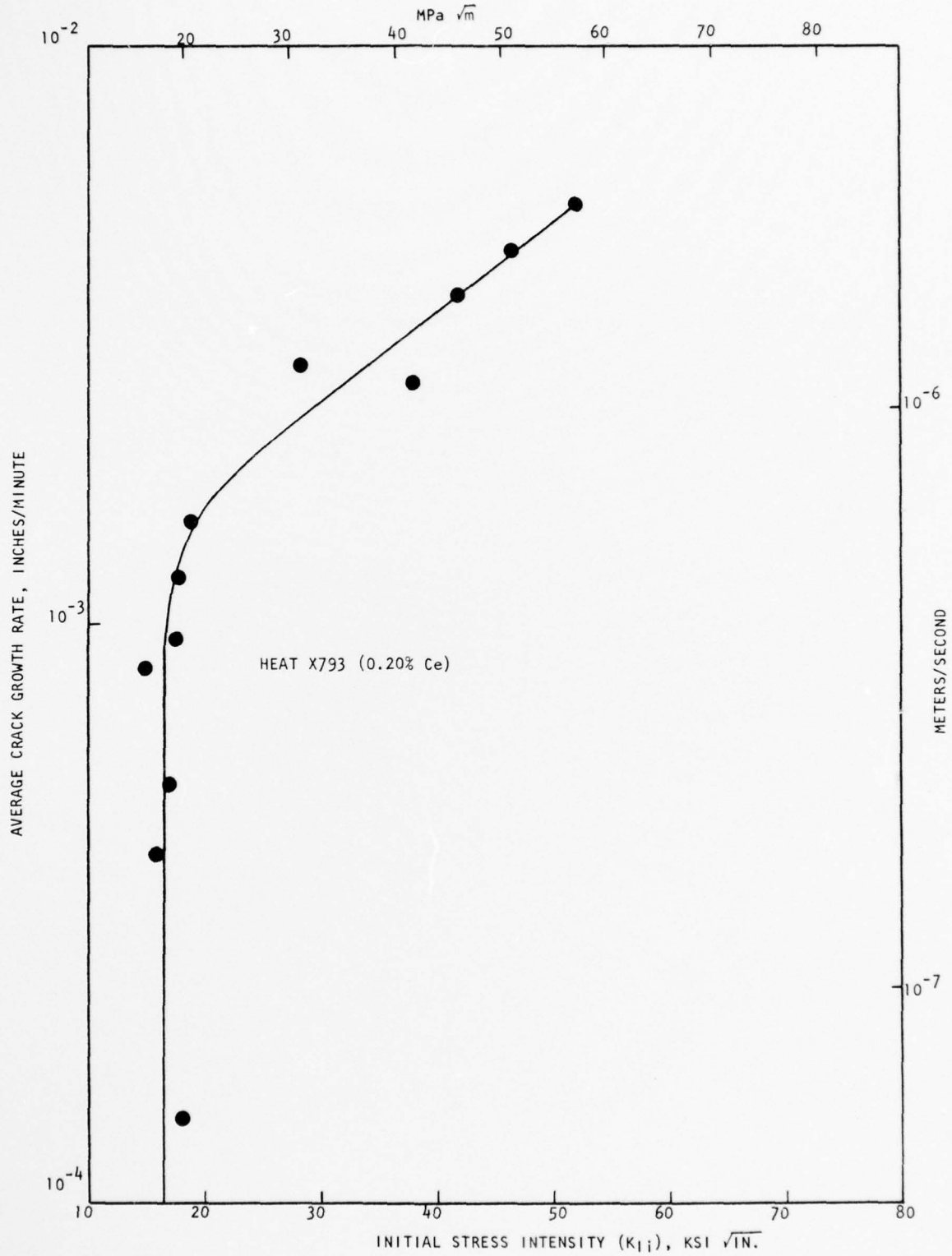

Figure 12. Stress corrosion crack growth rate as a function of initial stress intensity for 4340 steel heat X793 containing 0.20% cerium.

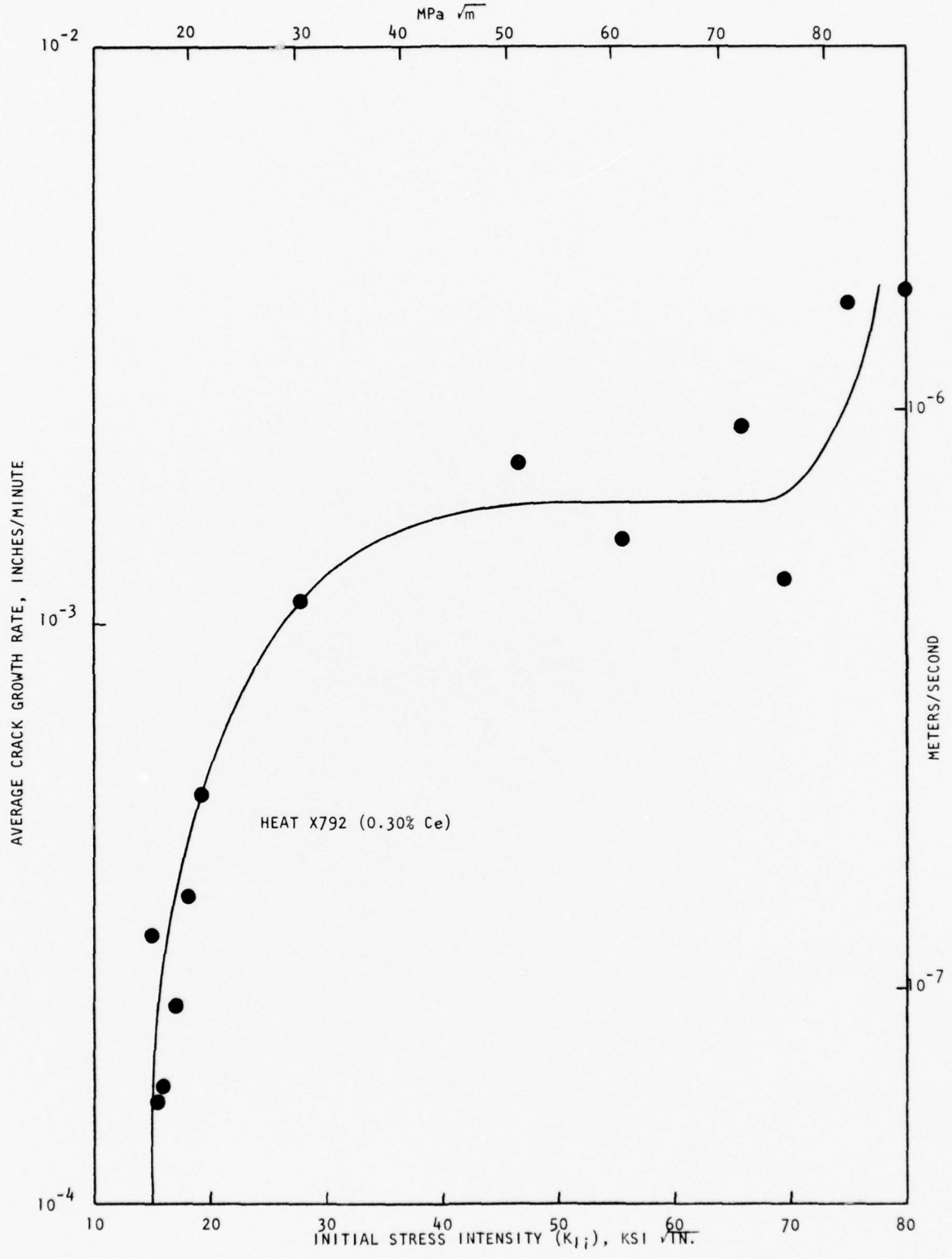

Figure 13. Stress corrosion crack growth rate as a function of initial stress intensity for 4340 steel heat X792 containing 0.30% cerium.

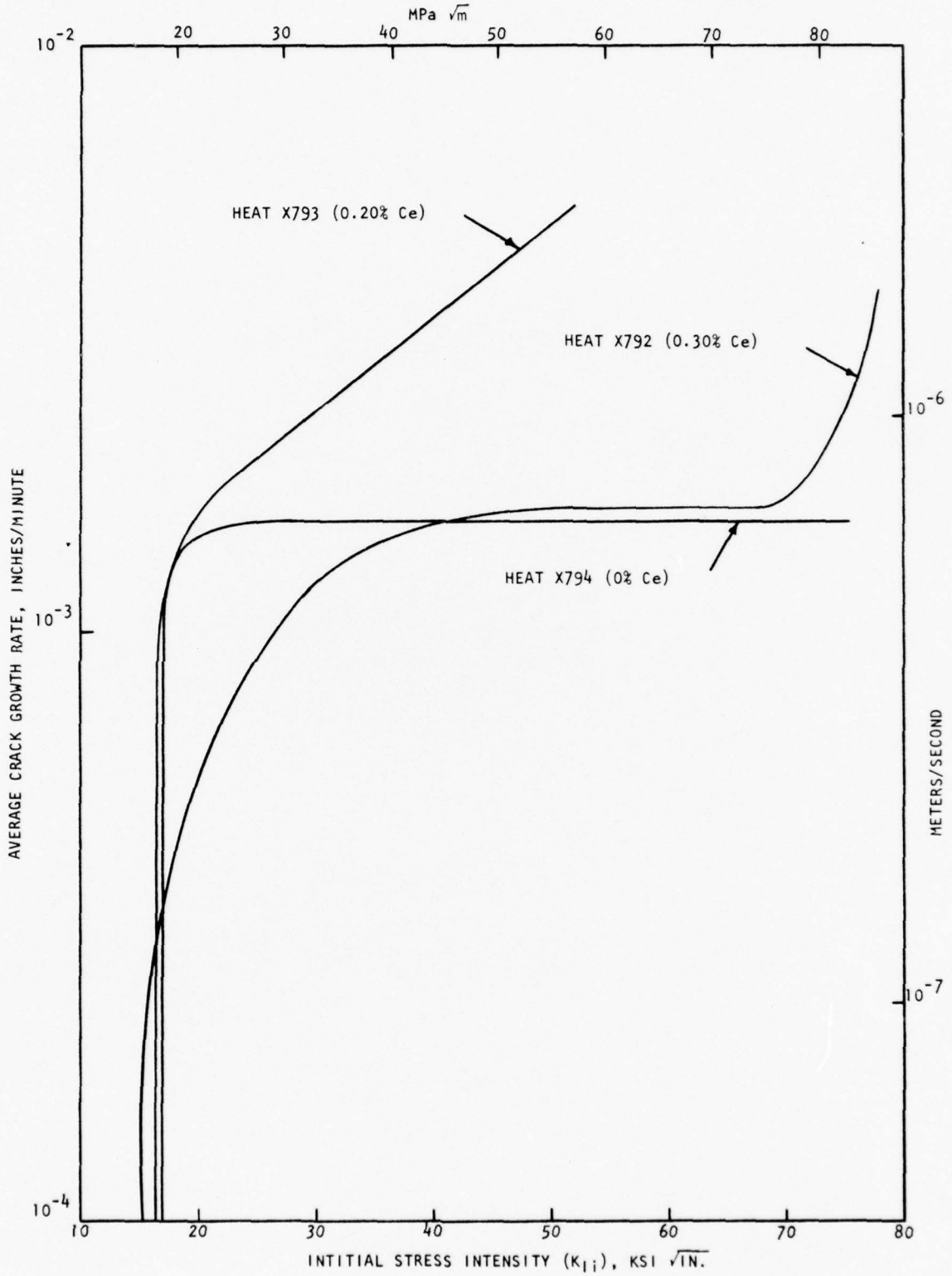

Figure 14. Comparison of stress corrosion crack growth rate versus K_{Ii} curves for 4340 steel with various cerium contents.

The effect of the cerium additions on stress corrosion cracking was much less pronounced than the effect of rare earth additions on internal hydrogen embrittlement observed in the previous work (7). The stress corrosion cracking threshold (K_{Iscc}) was about the same for all three materials, ranging fom 15 to 17 ksi $\sqrt{in.}$ (16.5 to 19 MPa $\sqrt{m}$). The higher cerium (0.30%) material had longer failure times (Figure 10) and lower average crack growth rates (Figure 14) than the lower cerium (0.20%) material. A valid comparison between the failure times and average crack growth rates for the steel without cerium and those for the two cerium-bearing steels could not be made because of crack branching, which occurred only in the material without cerium. A typical example of stress corrosion crack branching in a specimen from heat X794 is shown in Figure 15. Branching reduces the actual stress intensity at the crack tip and hence retards the rate of crack growth and increases the time to failure (13). For example, in a study of the effects of electrochemical variables on stress corrosion cracking in 4340 steel (14), for precracked cantilever bend specimens tested at the same K_{Ii} level and under identical environmental conditions, the failure times were 7.5 times longer when the crack branched than when branching did not occur. Crack branching was suppressed in the latter specimens by the use of deep side grooves (15). On this basis, it is estimated that, in the absence of branching, the failure times for the non-cerium steel would be shorter and the average crack growth rates higher than those for the lower cerium steel. It should be noted that crack branching cannot be relied upon to retard stress corrosion crack growth in service applications because branching may be suppressed by the structural configuration.

In the previous study of the effect of rare earth additions on the internal hydrogen embrittlement resistance of 4340 steel (7), it was found that the addition of either 0.17 weight percent cerium or 0.16 weight percent lanthanum resulted in an increase in the hydrogen embrittlement cracking threshold stress intensity by a factor of about four and a reduction of the crack growth rate by about an order of magnitude. These results were attributed to the ability of the rare earth elements to interact with hydrogen, thus reducing the supply of hydrogen available for embrittlement and impeding the diffusion of hydrogen to the crack tip where it would accumulate and cause crack growth by local embrittlement. At a given stress intensity level, a critical hydrogen concentration is required at the crack tip to initiate and sustain crack growth in high strength steels (16-18). As the crack tip hydrogen concentration is reduced, the stress intensity required to initiate crack growth (i.e., the hydrogen embrittlement cracking threshold) increases. Thus, the threshold stress intensities of the rare earth treated 4340 steels were much higher than that of the standard 4340 steel because of the greatly reduced hydrogen concentration at the crack tip. Once crack growth has initiated, the rate of crack growth at any given stress intensity level above the threshold depends on the rate at which hydrogen is transported to the tip of the crack. Thus, the crack growth rates in the rare earth treated 4340 steels were much lower than those in the standard 4340 steel because of the retardation of the diffusion of hydrogen to the crack tip.

The stress corrosion cracking results differed from the internal hydrogen embrittlement cracking behavior because the source of hydrogen was not the same, resulting in differences in the amount of hydrogen available for embrittlement and in the hydrogen transport processes. In the internal hydrogen embrittlement study, the specimens were electrolytically charged with hydrogen and plated with cadmium to contain the hydrogen in the metal. Thus, hydrogen was already present in the metal prior to sustained load testing, but in the rare earth treated steel specimens, the supply

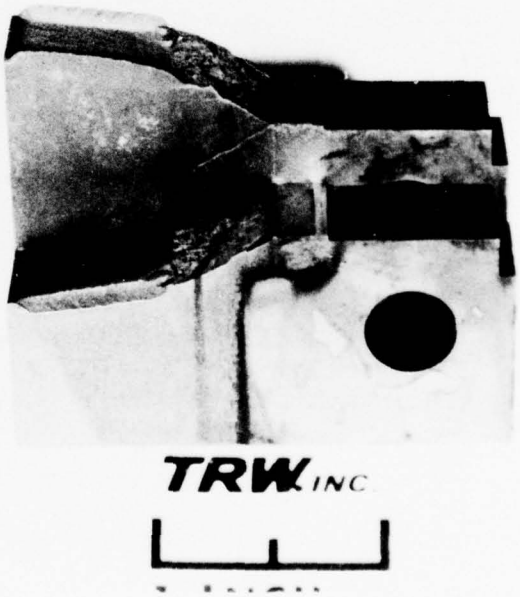

Figure 15. Typical example of stress corrosion crack branching in a specimen (No. 14) from Heat X794 (0% Ce).

of hydrogen available for embrittlement was reduced by the interaction of hydrogen with the rare earth elements. However, for the stress corrosion specimens, hydrogen entered the metal at the crack tip from the corrodent within the crack, so that the supply of hydrogen available for embrittlement was unlimited in both the rare earth treated and standard steel specimens. Because of this, there were no differences in the stress corrosion cracking thresholds of the three steels. In the internal hydrogen embrittlement study, the hydrogen transport process in the hydrogen-charged specimens consisted of diffusion through the bulk metal to the tip of the crack, but in the rare earth treated steel specimens, hydrogen diffusion was retarded by the presence of the rare earths. In environmental hydrogen embrittlement, the path of the diffusion of hydrogen into the crack tip is very short and hydrogen transport is strongly influenced by metal-environment reactions. Thus, the kinetics of stress corrosion crack growth in high strength steels are controlled by the surface reactions at the tip of the crack (19). Because of this, the increase in failure times and the decrease in crack growth rates resulting from the rare earth additions in the stress corrosion cracking study were much smaller than the corresponding changes in the internal hydrogen embrittlement study.

C. Fractographic Analysis

Fractographic examination was performed on six of the failed stress corrosion test specimens, two from each of the three steels, one of these having been tested at a low initial stress intensity level (15.4 to 17.0 ksi $\sqrt{in.}$) and one having been tested at a high initial stress intensity level (52.1 to 57.2 ksi $\sqrt{in.}$). These were specimens 10 and 14 from heat X794 (0% Ce), specimens 7 and 15 from heat X793 (0.20% Ce), and specimens 6 and 12 from heat X792 (0.30% Ce).

The fracture surfaces of the three specimens tested at low K_{Ii} levels are shown in Figure 16. The stress corrosion cracking area has a granular appearance in all three specimens. The rapid fracture area contains longitudinal ridges only in the two specimens containing cerium. These ridges resulted from separation along the rare earth oxide inclusions (Figure 17) which were elongated by the forging and hot rolling processes. In the specimen with no cerium, the stress corrosion crack appears to have begun to branch just prior to the onset of rapid fracture.

The fracture surfaces of the three specimens tested at high K_{Ii} levels are shown in Figure 18. In the two specimens containing cerium, both the stress corrosion cracking and rapid fracture areas contain longitudinal ridges. The presence of these ridges in the stress corrosion cracking area is probably due to the high stress intensity levels during stress corrosion cracking in these specimens, which resulted in separation along the rare earth oxide inclusions (Figure 6) such as occurred in the rapid fracture area. In the specimen with no cerium, the stress corrosion crack branched directly from the end of the fatigue precrack. Two other views of this specimen are shown in Figure 15.

Scanning electron microscope photographs of the fracture surfaces of the six specimens were taken at various distances from the end of the fatigue precrack along the centerline of he fracture surface, i.e. at the mid-thickness of the specimen. Fractographs of the three specimens tested at low initial stress intensity levels are shown in Figures 19, 20, and 21. The morphology of stress corrosion crack propagation was the same in all three specimens. At shorter crack lengths and corresponding low K levels, the morphology was almost entirely intergranular (Figures 19 a-d, 20 a-d, and 21 a-c). With increasing crack length and K level, the proportion of dimpled rupture

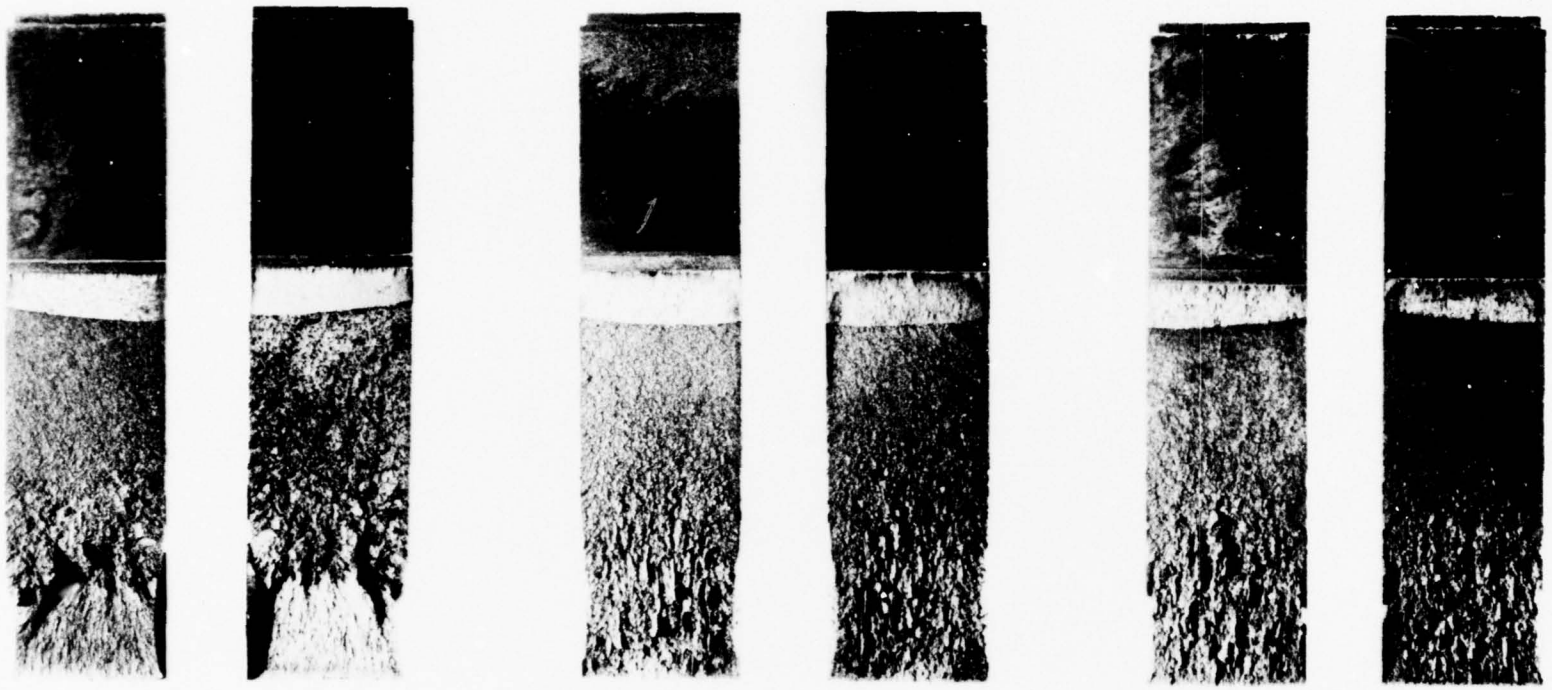

(a) Specimen 10, Heat X794 (0% Ce) K_{Ii} = 15.7 ksi$\sqrt{in.}$ (17.2 MPa$\sqrt{m}$)

(b) Specimen 7, Heat X793 (0.20% Ce) K_{Ii} = 17.0 ksi$\sqrt{in.}$ (18.7 MPa$\sqrt{m}$)

(c) Specimen 6, Heat X792 (0.30% Ce) K_{Ii} = 15.4 ksi$\sqrt{in.}$ (16.9 MPa$\sqrt{m}$)

Figure 16. Fracture surfaces of specimens tested at low initial stress intensity (K_{Ii}) levels. Magnification 2X.

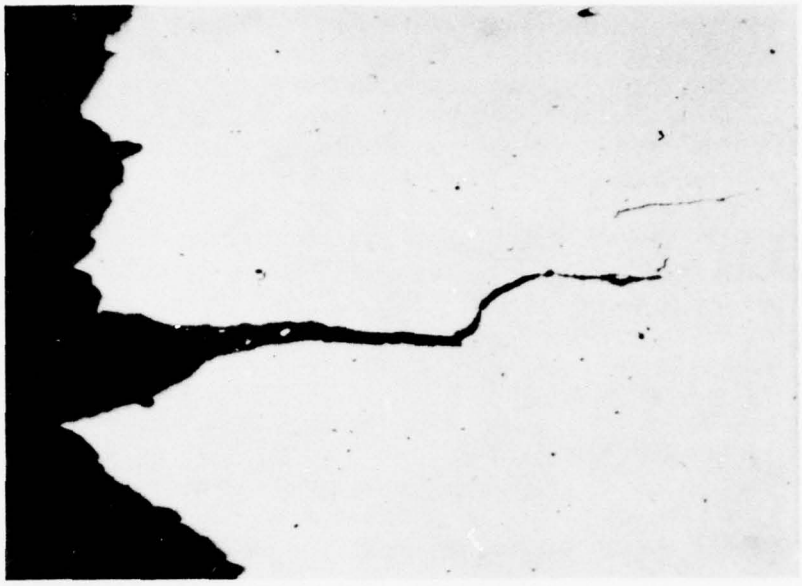

Magnification, 125X

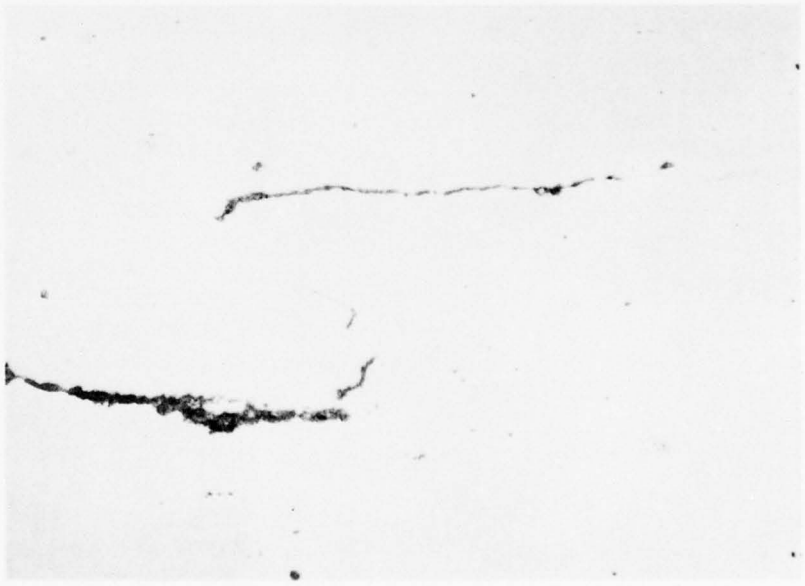

Magnification, 400X

Figure 17. Separation along rare earth oxide inclusions in Specimen 8 from 4340 steel Heat X792 (0.30% Ce), resulting in longitudinal ridges on fracture surface (left of upper photograph). Plane of plate is horizontal.

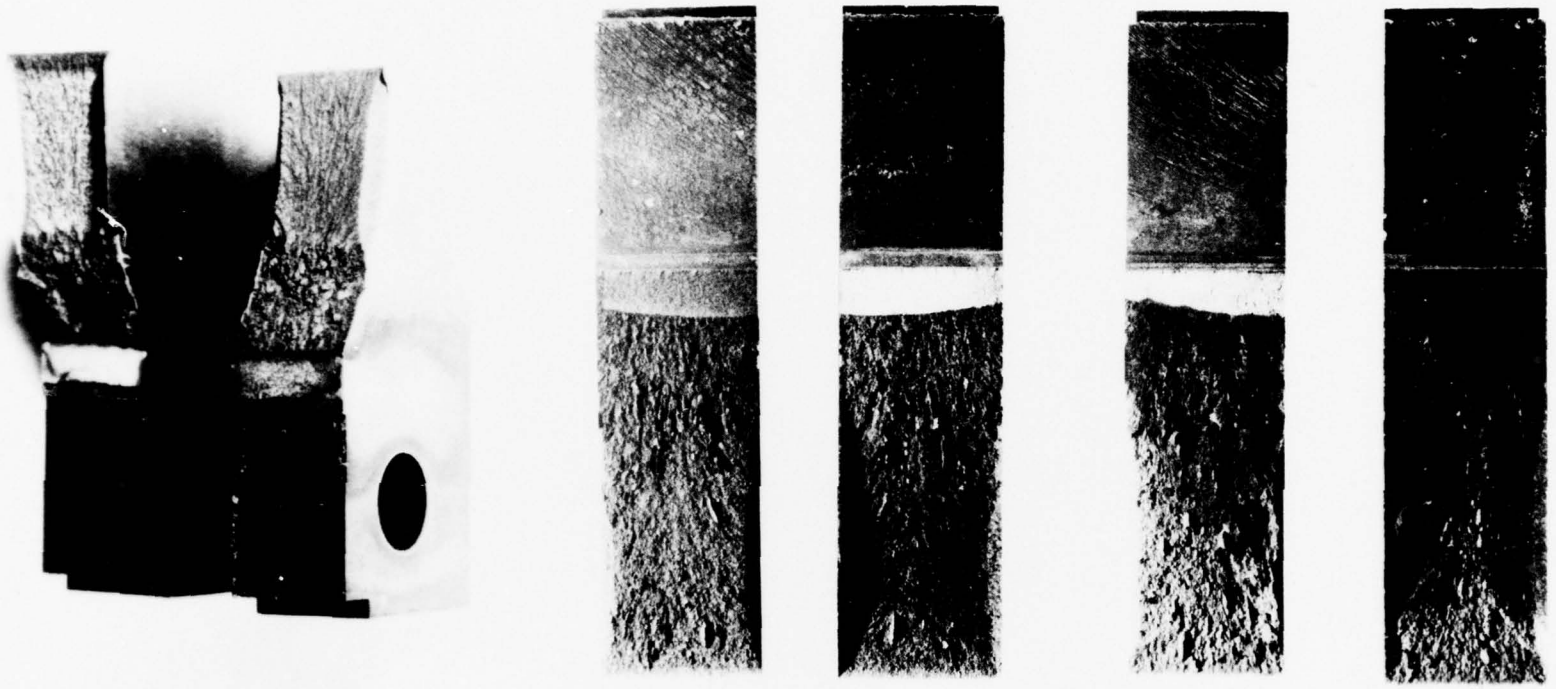

(a) Specimen 14, Heat X794 (0% Ce) K_{Ii} = 57.2 ksi$\sqrt{in.}$ (62.9 MPa$\sqrt{m}$)

(b) Specimen 15, Heat X793 (0.20% Ce) K_{Ii} = 52.1 ksi$\sqrt{in.}$ (57.2 MPa$\sqrt{m}$)

(c) Specimen 12, Heat X792 (0.30% Ce) K_{Ii} = 55.4 ksi$\sqrt{in.}$ (60.9 MPa$\sqrt{m}$)

Figure 18. Fracture surfaces of specimens tested at high initial stress intensity (K_{Ii}) levels. Magnification, (a) 1.5X, (b) and (c) 2X.

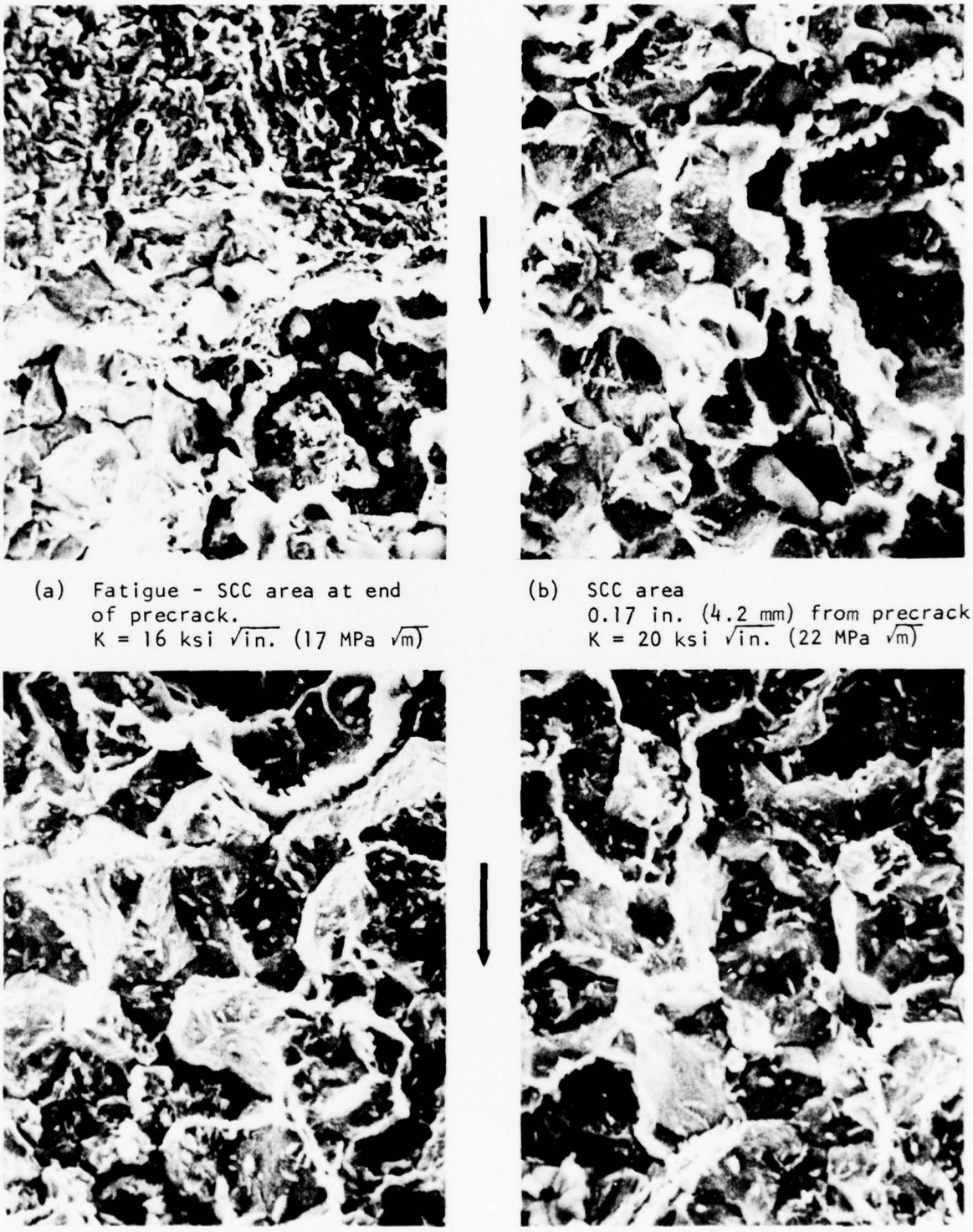

(a) Fatigue - SCC area at end of precrack.
K = 16 ksi $\sqrt{in.}$ (17 MPa $\sqrt{m}$)

(b) SCC area
0.17 in. (4.2 mm) from precrack
K = 20 ksi $\sqrt{in.}$ (22 MPa $\sqrt{m}$)

(c) SCC area
0.33 in. (8.4 mm) from precrack
K = 26 ksi $\sqrt{in.}$ (29 MPa $\sqrt{m}$)

(d) SCC area
0.49 in. (12.5 mm) from precrack
K = 38 ksi $\sqrt{in.}$ (42 MPa $\sqrt{m}$)

Figure 19. Fractographs of Specimen 10 from Heat X794 (0% Ce). Arrows indicate direction of crack propagation. Magnification, 1000X.

(e) SCC area
0.66 in. (16.8 mm) from precrack
K = 60 ksi $\sqrt{in.}$ (66 MPa $\sqrt{m}$)

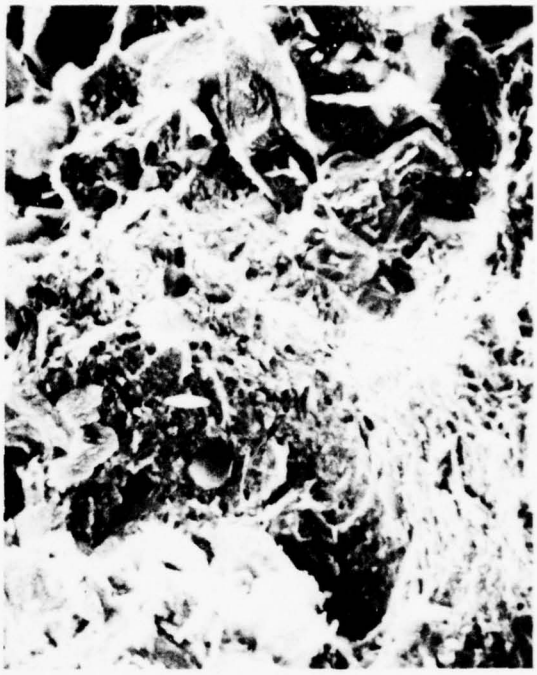

(f) SCC area
0.73 in. (18.6 mm) from precrack
K = 75 ksi $\sqrt{in.}$ (83 MPa $\sqrt{m}$)

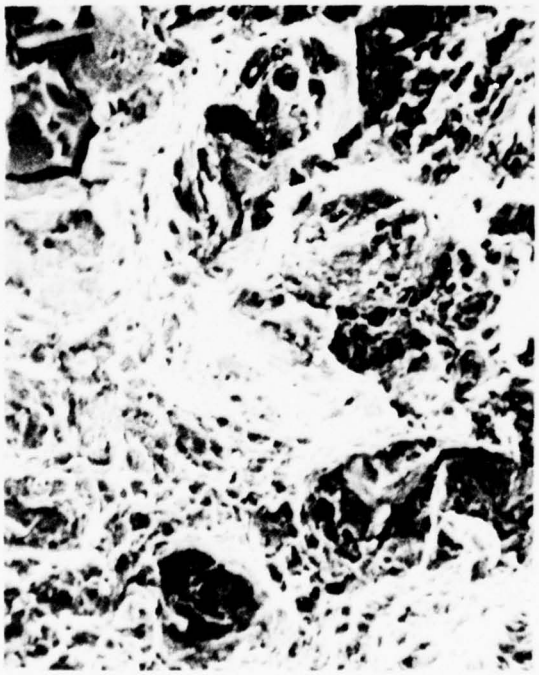

(g) SCC area
0.81 in. (20.5 mm) from precrack
K = 99 ksi $\sqrt{in.}$ (109 MPa $\sqrt{m}$)

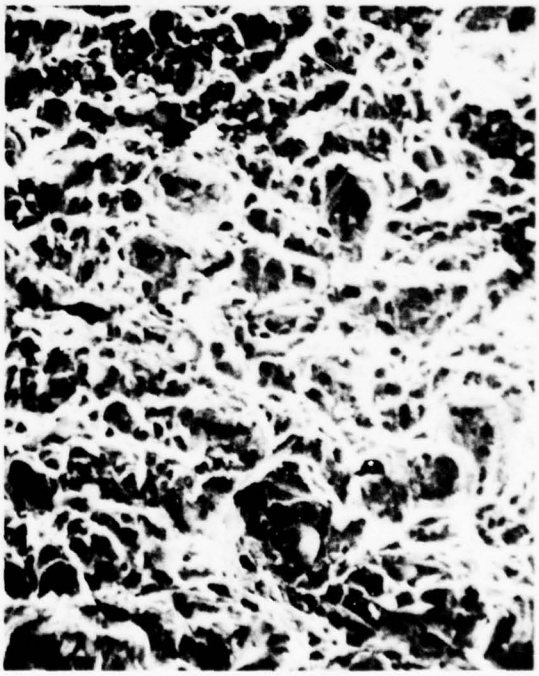

(h) Rapid fracture area
1.12 in. (28.5 mm) from precrack

Figure 19. (continued).

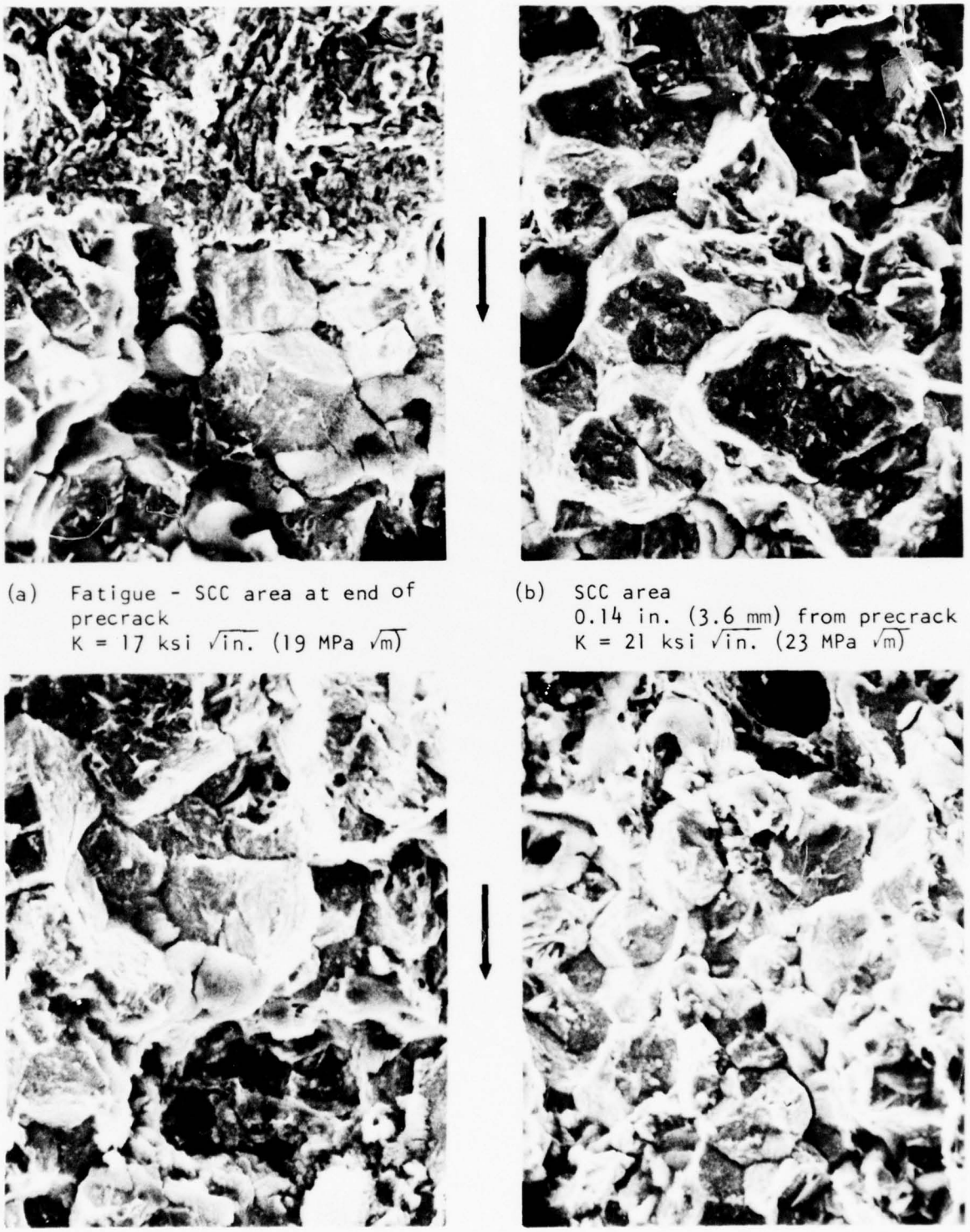

(a) Fatigue - SCC area at end of precrack
K = 17 ksi $\sqrt{in.}$ (19 MPa $\sqrt{m}$)

(b) SCC area
0.14 in. (3.6 mm) from precrack
K = 21 ksi $\sqrt{in.}$ (23 MPa $\sqrt{m}$)

(c) SCC area
0.28 in. (7.1 mm) from precrack
K = 27 ksi $\sqrt{in.}$ (29 MPa $\sqrt{m}$)

(d) SCC area
0.42 in. (10.7 mm) from precrack
K = 35 ksi $\sqrt{in.}$ (39 MPa $\sqrt{m}$)

Figure 20. Fractographs of Specimen 7 from Heat X793 (0.20% Ce). Arrows indicate direction of crack propagation. Magnification, 1000X

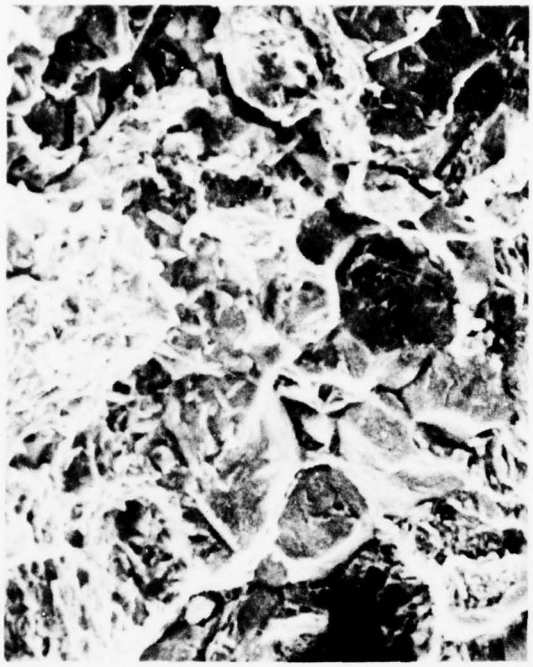

(e) SCC area
0.56 in. (14.3 mm) from precrack
K = 51 ksi $\sqrt{in.}$ (56 MPa $\sqrt{m}$)

(f) SCC area
0.66 in. (16.9 mm) from precrack
K = 69 ksi $\sqrt{in.}$ (76 MPa $\sqrt{m}$)

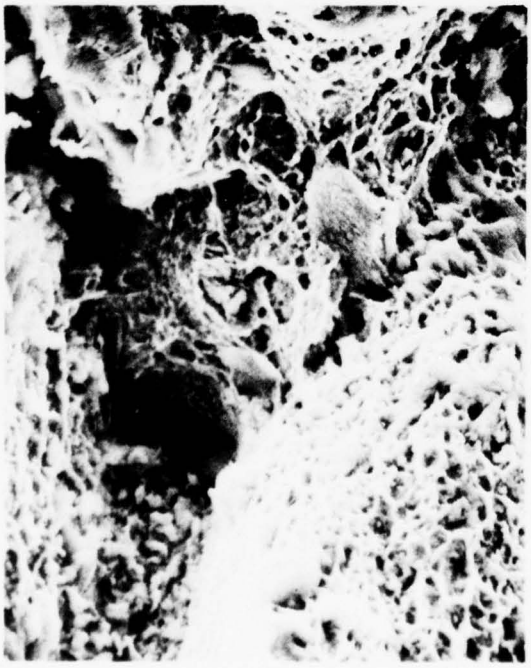

(g) SCC area
0.77 in. (19.5 mm) from precrack
K = 100 ksi $\sqrt{in.}$ (110 MPa $\sqrt{m}$)

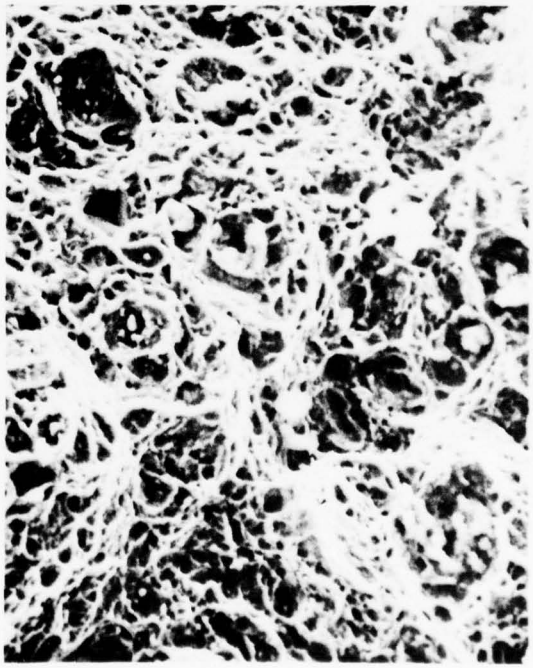

(h) Rapid fracture area
0.98 in. (25.0 mm) from precrack

Figure 20. (continued).

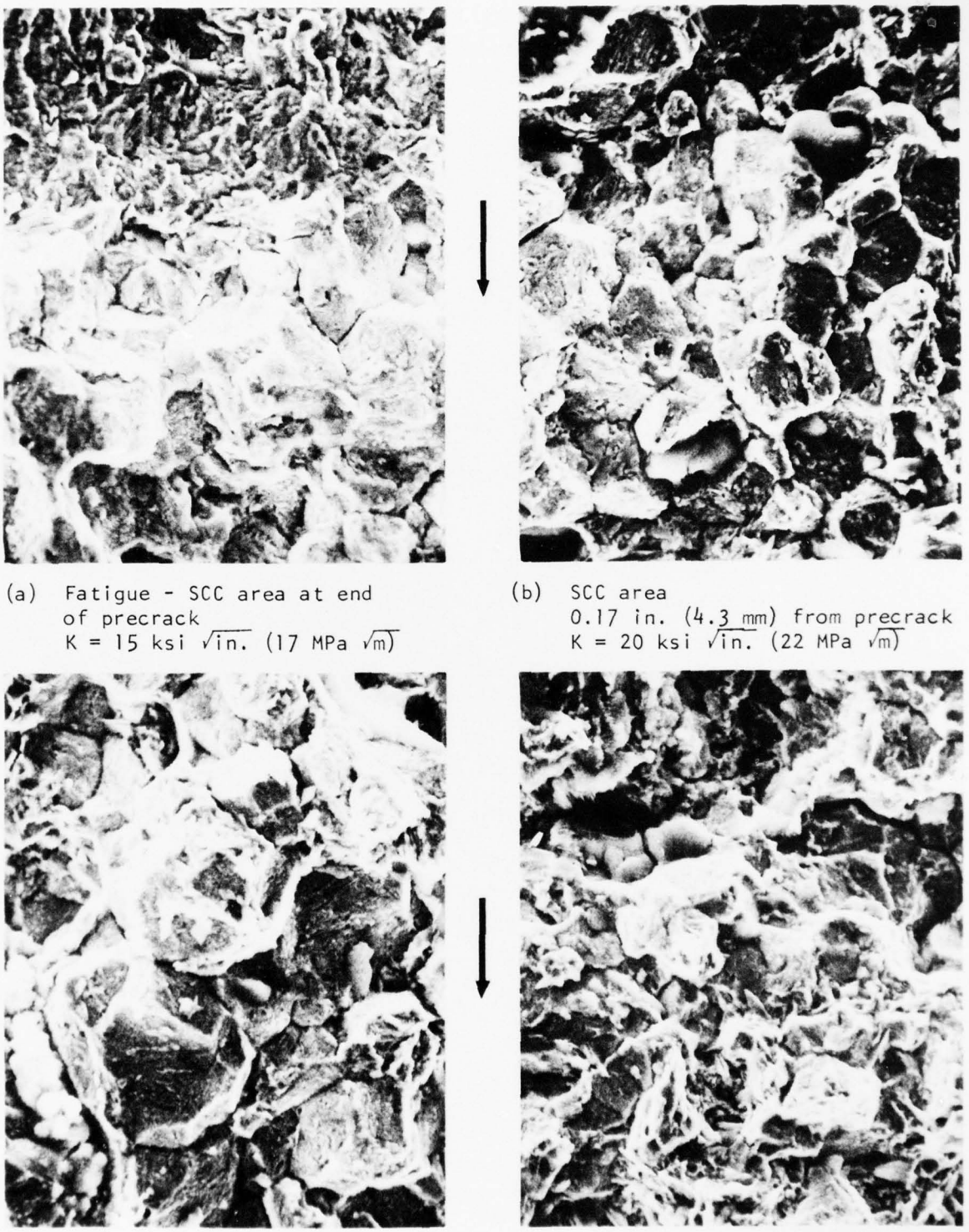

(a) Fatigue - SCC area at end of precrack
K = 15 ksi $\sqrt{in.}$ (17 MPa $\sqrt{m}$)

(b) SCC area
0.17 in. (4.3 mm) from precrack
K = 20 ksi $\sqrt{in.}$ (22 MPa $\sqrt{m}$)

(c) SCC area
0.33 in. (8.5 mm) from precrack
K = 26 ksi $\sqrt{in.}$ (29 MPa $\sqrt{m}$)

(d) SCC area
0.50 in. (12.8 mm) from precrack
K = 37 ksi $\sqrt{in.}$ (41 MPa $\sqrt{m}$)

Figure 21. Fractographs of Specimen 6 from Heat X792 (0.30% Ce). Arrows indicate direction of crack propagation. Magnification, 1000X

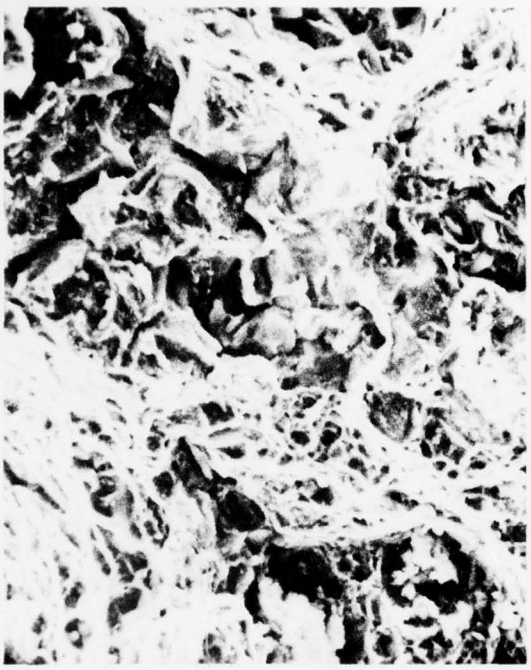

(e) SCC area
0.63 in. (15.9 mm) from precrack
K = 53 ksi $\sqrt{in.}$ (58 MPa $\sqrt{m}$)

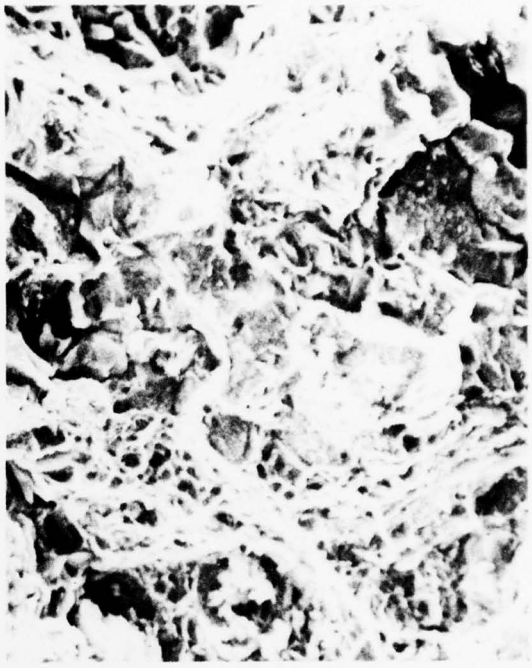

(f) SCC area
0.67 in. (17.0 mm) from precrack
K = 60 ksi $\sqrt{in.}$ (66 MPa $\sqrt{m}$)

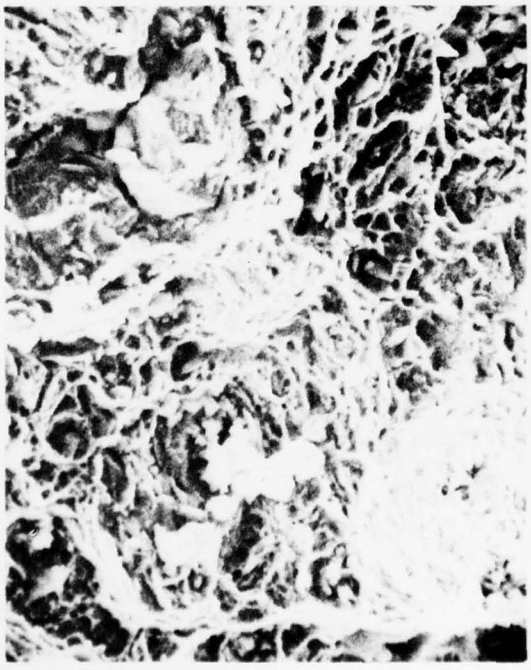

(g) SCC area
0.79 in. (20.0 mm) from precrack
K = 90 ksi $\sqrt{in.}$ (99 MPa $\sqrt{m}$)

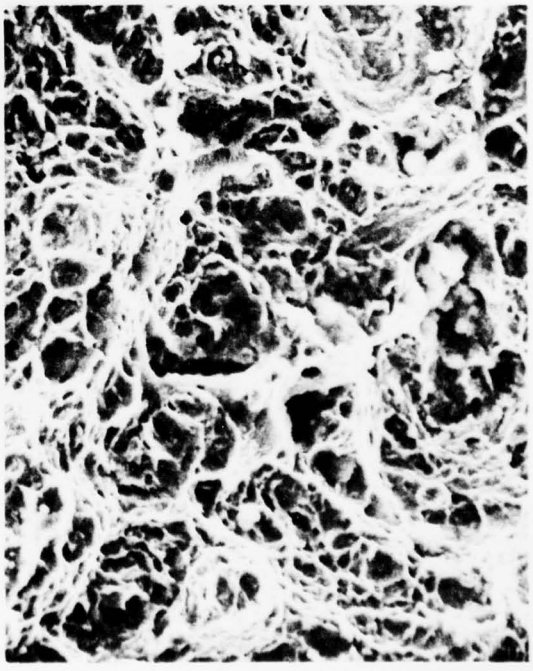

(h) Rapid fracture area
1.13 in. (28.8 mm) from precrack

Figure 21. (continued).

gradually increased (Figures 19 c-g, 20 c-g, and 21 c-g), up to the onset of rapid fracture. In the rapid fracture area, the crack propagation morphology was entirely dimpled rupture in all three specimens (Figures 19h, 20h, and 21h). The stress corrosion crack propagation morphology of the three specimens tested at high initial stress intensity levels was similar to that of the three specimens tested at low K_{Ii} levels, except that the proportion of dimpled rupture was higher at any given crack length which, in these specimens, corresponded to higher K levels.

Thus, the fractographic analysis showed that a predominantly intergranular morphology was associated with low stress intensity levels, with an increasing proportion of dimpled rupture as the stress intensity level increased. This fractographic morphology is typical of stress corrosion cracking in high strength, low alloy, martensitic steels (20).

IV SUMMARY AND CONCLUSIONS

The addition of the rare earth element cerium to AISI 4340 steel was investigated as a means of improving its stress corrosion cracking resistance. Previous work had shown that rare earth additions at levels of approximately 0.2 weight percent substantially improved the internal hydrogen embrittlement resistance of this steel. Because the stress corrosion cracking resistance of high strength steels such as 4340 is believed to be strongly related to their hydrogen embrittlement resistance, this study was undertaken to extend the concept of rare earth additions to stress corrosion behavior. The experimental approach involved the preparation of three 50-pound (23-kg) heats of 4340 steel containing zero, 0.20 and 0.30 weight percent cerium which were vacuum-induction melted and hot worked into plate form. The test material was heat treated to a yield strength level of approximately 215 ksi (1480 MPa). The resistance to stress corrosion cracking was characterized by conducting sustained load tests on fatigue-precracked compact tension specimens in 3.5 percent sodium chloride solution at room temperature.

The cerium additions had a much smaller effect on the stress corrosion cracking resistance than cerium and lanthanum additions had on the internal hydrogen embrittlement resistance in the previous study. The stress corrosion cracking threshold (K_{Iscc}) was about the same for all three steels, ranging from 15 to 17 ksi $\sqrt{in.}$ (16.5 to 19 MPa$\sqrt{m}$). The higher cerium (0.30%) material had longer failure times and lower average crack growth rates than the lower cerium (0.20%) material. The failure times and average crack growth rates for the steel without cerium could not be directly compared with those for the two cerium-bearing steels because of crack branching, which occurred only in the material without cerium. However, it was estimated that, in the absence of branching, the failure times for the non-cerium steel would be shorter and the average crack growth rates higher than those for the lower cerium steel.

The difference between the effects of the rare earth additions on stress corrosion cracking and internal hydrogen embrittlement was attributed to the difference in the source of hydrogen in the two cracking phenomena, which affects the amount of hydrogen available for embrittlement and the processes of hydrogen transport to the tip of the crack. In internal hydrogen embrittlement, hydrogen is already present in the metal prior to sustained loading, so that the supply of available hydrogen is limited and hydrogen transport to the crack tip occurs by diffusion through the bulk metal, which was affected by the presence of the rare earths. However, in stress corrosion cracking, hydrogen enters the metal at the crack tip from the corrodent within the crack during sustained loading, so that the supply of available hydrogen is unlimited and hydrogen transport into the crack tip is strongly influenced by metal-environment reactions at the crack tip surface, which were only mildly affected by the presence of the rare earths. The fractographic morphology of stress corrosion crack propagation for all three steels was intergranular at low stress intensity levels, with an increasing proportion of dimpled rupture as the stress intensity level increased.

V REFERENCES

1. H. L. Logan, The Stress Corrosion of Metals, John Wiley and Sons, New York, 1966, pp. 70-99.

2. E. H. Phelps, "A Review of the Stress Corrosion Behavior of Steels with High Yield Strength," Proceedings of Conference, Fundamental Aspects of Stress Corrosion Cracking, R. W. Staehle, A. J. Forty, and D. van Rooyen, eds., National Association of Corrosion Engineers, Houston, 1969, pp. 398-410.

3. B. F. Brown, "Stress Corrosion Cracking of High Strength Steels," in The Theory of Stress Corrosion Cracking in Alloys, J. C. Scully, ed., NATO Scientific Affairs Division, Brussels, 1971, pp. 186-204.

4. G. Sandoz, "High Strength Steels," Chapter 3 of Stress-Corrosion Cracking in High Strength Steels and in Titanium and Aluminum Alloys, B. F. Brown, ed., U.S. Naval Research Laboratory, Washington, D.C., 1972, pp. 79-145.

5. C. F. Barth, E. A. Steigerwald and A. R. Troiano, "Hydrogen Permeability and Delayed Failure of Polarized Martensitic Steels," Corrosion, Vol. 25, No. 9, September 1969, pp. 353-358.

6. J. A. Smith, M. H. Peterson and B. F. Brown, "Electrochemical Conditions at the Tip of an Advancing Stress Corrosion Crack in AISI 4340 Steel," Corrosion, Vol. 26, No. 12, December 1970, pp. 539-542.

7. C. S. Kortovich, "Inhibition of Hydrogen Embrittlement in High Strength Steel," TRW Technical Report No. ER-7814-2, prepared for ONR Contract No. N00014-74-C-0365, February 1977.

8. C. S. Carter, "The Effect of Silicon on the Stress Corrosion Resistance of Low Alloy High Strength Steels," Corrosion, Vol. 25, No. 10, October 1969, pp. 423-431.

9. G. Sandoz, "The Effects of Alloying Elements on the Susceptibility to Stress-Corrosion Cracking of Martensitic Steels in Salt Water," Met. Trans., Vol. 2, No. 4, April 1971, pp. 1055-1063.

10. M. H. Peterson, B. F. Brown, R. L. Newbegin and R.E. Groover, "Stress Corrosion Cracking of High Strength Steels and Titanium Alloys in Chloride Solutions at Ambient Temperature," Corrosion, Vol. 23, No. 5, May 1967, pp. 142-148.

11. "Standard Test Method for Plane-Strain Fracture Toughness of Metallic Materials," ASTM E 399-74, 1977 Annual Book of ASTM Standards, Part 10, American Society for Testing and Materials, Philadelphia, 1977, pp. 505-524.

12. U.S. Military Specification, "Steel Bars, Reforging Stock, and Mechanical Tubing, Low Alloy, Premium Quality," MIL-S-8844C, May 25, 1971.

13. I. M. Austen, R. Brook, and J. M. West, "Effective Stress Intensities in Stress Corrosion Cracking," Intl. Journal of Fracture, Vol. 12, No. 2, April 1976, pp. 253-263.

14. A. A. Sheinker, unpublished research performed at Lehigh University, 1972.

15. A. A. Sheinker, "The Effects of Electrochemical Variables on the Kinetics of Stress Corrosion Cracking in AISI 4340 Steel," Ph.D. Dissertation, Lehigh University, 1972.

16. A. R. Troiano, "The Role of Hydrogn and Other Interstitials in the Mechanical Behavior of Metals, Trans. ASM, Vol. 52, 1960, pp. 54-80.

17. R. A. Oriani, "A Mechanistic Theory of Hydrogen Embrittlement of Steels," Berichte der Bunsen-Gesellschaft fur Physikalische Chemie, Vol. 76, 1972, pp. 848-857.

18. W. W. Gerberich and Y. T. Chen, "Hydrogen-Controlled Cracking - - An Approach to Threshold Stress Intensity," Met. Trans. A, Vol. 6A, No. 2, February 1975, pp. 271-278.

19. M. Pourbaix, "Electrochemical Aspects of Stress Corrosion Cracking," in The Theory of Stress Corrosion Cracking in Alloys, J. C. Scully, ed., NATO Scientific Affairs Division, Brussels, 1971, pp. 17-61.

20. C. D. Beachem, "A New Model for Hydrogen-Assisted Cracking (Hydrogen "Embrittlement")," Met. Trans., Vol. 3, No. 2, February 1972, pp. 437-451.

BASIC DISTRIBUTION LIST

Technical and Summary Reports

Organization	No. of Copies
Defense Documentation Center Cameron Station Alexandria, Virginia 22314	(12)
Office of Naval Research Department of the Navy	
Attn: Code 471	(1)
Code 102	(1)
Code 470	(1)
Commanding Officer Office of Naval Research Branch Office 495 Summer Street Boston, Massachusetts 02210	(1)
Commanding Officer Office of Naval Research Branch Office 536 South Clark Street Chicago, Illinois 60605	(1)
Office of Naval Research San Francisco Area Office 760 Market Street, Room 447 San Francisco, California 94102 Attn: Dr. P. A. Miller	(1)
Naval Research Laboratory Washington, D.C. 20390	
Attn: Code 6000	(1)
Code 6100	(1)
Code 6300	(1)
Code 6400	(1)
Code 2627	(1)
Naval Air Development Center Code 302 Warminster, Pennsylvania 18974 Attn: Mr. F. S. Williams	(1)
Naval Air Propulsion Test Center Trenton, New Jersey 08628 Attn: Library	(1)
Naval Construction Battallion Civil Engineering Laboratory Port Hueneme California 93043 Attn: Materials Division	(1)
Naval Electronics Laboratory Center San Diego, California 92152 Attn: Electron Materials Sciences Division	(1)
Naval Missile Center Materials Consultant Code 3312-1 Point Mugu, California 93041	(1)
Commanding Officer Naval Surface Weapons Center White Oak Laboratory Silver Spring, Maryland 20910 Attn: Library	(1)
David W. Taylor Naval Ship R&D Center Materials Department Annapolis, Maryland 21402	(1)
Naval Undersea Center San Diego, California 92132 Attn: Library	(1)
Naval Underwater System Center Newport, Rhode Island 02840 Attn: Library	(1)
Naval Weapons Center China Lake, California 93555 Attn: Library	(1)
Naval Postgraduate School Monterey, California 93940 Attn: Mechanical Engr. Dept.	(1)
Naval Air Systems Command Washington, D.C. 20360	
Attn: Code 52031	(1)
Code 52032	(1)
Code 320	(1)

BASIC DISTRIBUTION LIST (Cont'd)

Organization	No. of Copies
Naval Sea System Command Washington, D.C. 20362 Attn: Code 035	(1)
Naval Facilities Engineering Command Alexandria, Virginia 22331 Attn: Code 03	(1)
Scientific Advisor Commandant of the Marine Corps Washington, D.C. 20380 Attn: Code AX	(1)
Naval Ship Engineering Center Department of the Navy CTR BG #2 3700 East-West Highway Prince Georges Plaza Hyattsville, Maryland 20782 Attn: Engineering Materials and Services Office, Code 6101	(1)
Army Research Office Box CM, Duke Station Durham, North Carolina 27706 Attn: Metallurgy & Ceramics Div.	(1)
Army Materials and Mechanics Research Center Watertown, Massachusetts 02172 Attn: Res. Programs Office (AMXMR-P)	(1)
Air Force Office of Scientific Research Bldg. 410 Bolling Air Force Base Washington, D.C. 20332 Attn: Chemical Science Directorate Electronics & Solid State Sciences Directorate	(1) (1)
Air Force Materials Lab (LA) Wright-Patterson AFB Dayton, Ohio 45433	(1)
NASA Headquarters Washington, D.C. 20546 Attn: Code RRM	(1)
NASA Lewis Research Center 21000 Brookpark Road Cleveland, Ohio 44135 Attn: Library	(1)
National Bureau of Standards Washington, D.C. 20234 Attn: Metallurgy Division Inorganic Materials Div.	(1) (1)
Defense Metals and Ceramics Information Center Battelle Memorial Institute 505 King Avenue Columbus, Ohio 43201	(1)
Director Ordnance Research Laboratory P.O. Box 30 State College, Pennsylvania 16801	(1)
Director Applied Physics Laboratory University of Washington 1013 Northeast Fortieth Street Seattle, Washington 98105	(1)
Metals and Ceramics Division Oak Ridge National Laboratory P.O. Box X Oak Ridge, Tennessee 37380	(1)
Los Alamos Scientific Laboratory P.O. Box 1663 Los Alamos, New Mexico 87544 Attn: Report Librarian	(1)
Argonne National Laboratory Metallurgy Division P.O. Box 229 Lemont, Illinois 60439	(1)

BASIC DISTRIBUTION LIST (cont'd)

Organization	No. of Copies	Organization	No. of Copies
Brookhaven National Laboratory Technical Information Division Upton, Long Island New York 11973 Attn: Research Library	(1)		
Library Building 50 Room 134 Lawrence Radiation Laboratory Berkeley, California	(1)		

SUPPLEMENTARY DISTRIBUTION LIST

Technical and Summary Reports

Professor G. S. Ansell
Rensselaer Polytechnic Institute
Dept. of Metallurgical Engineering
Troy, New York 12181

Professor Dieter G. Ast
Cornell University
Department of Materials Science
and Engineering
College of Engineering, Bard Hall
Ithaca, New York 14853

Professor H. K. Birnbaum
University of Illinois
Department of Metallurgy
Urbana, Illinois 61801

Dr. E. M. Breinan
United Technologies
Research Center
East Hartford, Connecticut 06108

Professor H. D. Brody
University of Pittsburgh
School of Engineering
Pittsburgh, Pennsylvania 15213

Dr. Arthur E. Clark
Naval Surface Weapons Center
Solid State Division
White Oak Laboratory
Silver Spring, Maryland 20910

Professor J. B. Cohen
Northwestern University
Dept. of Material Sciences
Evanston, Illinois 60201

Professor M. Cohen
Massachusetts Institute of Technology
Department of Metallurgy
Cambridge, Massachusetts 02139

Dr. Ronald B. Diegle
505 King Avenue
Columbus, Ohio 43201

Mr. G. A. DiPietro
Advanced Vacuum Systems
30 Faulkner Street
Ayer, Massachusetts 01432

Professor Thomas W. Eagar
Massachusetts Institute of Technology
Department of Materials Science
and Engineering
Cambridge, Massachusetts 02139

Professor B. C. Giessen
Northeastern University
Department of Chemistry
Boston, Massachusetts 02115

Dr. G. T. Hahn
Battelle Memorial Institute
Department of Metallurgy
505 King Avenue
Columbus, Ohio 43201

Dr. David G. Howden
Battelle Memorial Institute
Columbus Laboratories
505 King Avenue
Columbus, Ohio 43201

Professor C. E. Jackson
Ohio State University
Dept. of Welding Engineering
190 West 19th Avenue
Columbus, Ohio 43210

Dr. Lyman A. Johnson
General Electric Company
P.O. Box 8
Schenectady, New York 12301

Dr. C. S. Kortovich
TRW Inc.
23555 Euclid Avenue
Cleveland, Ohio 44117

Professor D. A. Koss
Michigan Technological University
College of Engineering
Houghton, Michigan 49931

SUPPLEMENTARY DISTRIBUTION LIST (cont'd)

Professor E. Laughlin
Carnegie-Mellon University
Schenley Park
Pittsburgh, Pennsylvania 15213

Professor A. Lawley
Drexel University
Dept. of Metallurgical Engineering
Philadelphia, Pennsylvania 19104

Dr. John Mahoney
Phrasor Technology
110 South Euclid Avenue
Pasadena, California 91101

Dr. H. Margolin
Polytechnic Institute of New York
333 Jay Street
Brooklyn, New York 11201

Professor K. Masabuchi
Massachusetts Institute of Technology
Department of Ocean Engineering
Cambridge, Massachusetts 02139

Dr. H. I. McHenry
National Bureau of Standards
Institute for Basic Standards
Boulder, Colorado 80302

Professor J. W. Morris, Jr.
University of California
College of Engineering
Berkeley, California 94710

Professor Ono
University of California
Materials Department
Los Angeles, California 90024

Dr. M. Pakstys
General Dynamics
Electric Boat Division
Eastern Point Road
Groton, Connecticut 06340

Dr. Neil E. Paton
Rockwell International
Science Center
1049 Camino Dos Rios
P.O. Box 1085
Thousand Oaks, California 91360

Professor R. M. Pelloux
Massachusetts Institute of Technology
Department of Materials
Science and Engineering
Cambridge, Massachusetts 02139

Mr. A. Pollack
David W. Taylor Naval Ship
Research & Development Center
Annapolis Laboratory
Annapolis, Maryland 21402

Dr. Karl M. Prewo
United Technologies Laboratories
United Technologies Corporation
East Hartford, Connecticut 06108

Professor David Roylance
Massachusetts Institute of Technology
77 Massachusetts Avenue
Cambridge, Massachusetts 02139

Professor W. F. Savage
Rensselaer Polytechnic Institute
School of Engineering
Troy, New York 12181

Dr. C. Shaw
Rockwell International Science Center
1049 Camino Dos Rios
P.O. Box 1085
Thousand Oaks, California 91360

Professor O.D. Sherby
Stanford University
Materials Sciences Division
Stanford, California 94300

SUPPLEMENTARY DISTRIBUTION LIST (Cont'd)

Dr. R. P. Simpson
Westinghouse Electric Corporation
Research and Development Center
Pittsburgh, Pennsylvania 15235

Dr. W. A. Spitzig
U.S. Steel Corporation
Research Laboratory
Monroeville, Pennsylvania 15146

Dr. E. A. Starke, Jr.
Georgia Institute of Technology
School of Chemical Engineering
Atlanta, Georgia 30332

Professor N. S. Stoloff
Rensselaer Polytechnic Institute
School of Engineering
Troy, New York 12181

Dr. E. R. Thompson
United Technologies Research Center
United Technologies Corporation
East Hartford, Connecticut 06108

Professor David Turnbull
Harvard University
Division of Engineering and
Applied Physics
Cambridge, Massachusetts 02139

Professor W. E. Wallace
University of Pittsburgh
Pittsburgh, Pennsylvania 15260

Dr. F. E. Wawner
University of Virginia
School of Engineering and
Applied Science
Charlottesville, Virginia 22901

Dr. C. R. Whitsett
McDonnell Douglas Research
McDonnell Douglas Corporation
St. Louis, Missouri 63166

Dr. J. C. Williams
Carnegie-Mellon University
Department of Metallurgy and
Materials Sciences
Schenley Park
Pittsburgh, Pennsylvania 15213

Professor H.G.F. Wilsdorf
University of Virginia
Charlottesville, Virginia 22903

Dr. M. A. Wright
University of Tennessee
Space Institute
Tullahoma, Tennessee 37388

SUPPLEMENTARY DISTRIBUTION LIST

Technical and Summary Reports

Dr. T. R. Beck
Electrochemical Technology Corporation
10035 31st Avenue, NE
Seattle, Washington 98125

Professor I. M. Bernstein
Carnegie-Mellon University
Schenley Park
Pittsburgh, Pennsylvania 15213

Professor H. K. Birnbaum
University of Illinois
Department of Metallurgy
Urbana, Illinois 61801

Dr. Otto Buck
Rockwell International
1049 Camino Dos Rios
P.O. Box 1085
Thousand Oaks, California 91360

Dr. David L. Davidson
Southwest Research Institute
8500 Culebra Road
P.O. Drawer 28510
San Antonio, Texas 78284

Dr. D. J. Duquette
Department of Metallurgical Engineering
Rensselaer Polytechnic Institute
Troy, New York 12181

Professor R. T. Foley
The American University
Department of Chemistry
Washington, D.C. 20016

Mr. G. A. Gehring
Ocean City Research Corporation
Tennessee Avenue & Beach Thorofare
Ocean City, New Jersey 08226

Dr. J.A.S. Green
Martin Marietta Corporation
1450 South Rolling Road
Baltimore, Maryland 21227

Professor R. H. Heidersbach
University of Rhode Island
Department of Ocean Engineering
Kingston, Rhode Island 02881

Professor H. Herman
State University of New York
Material Sciences Division
Stony Brook, New York 11794

Professor J. P. Hirth
Ohio State University
Metallurgical Engineering
Columbus, Ohio 43210

Dr. D. W. Hoeppner
University of Missouri
College of Engineering
Columbia, Missouri 65201

Dr. E. W. Johnson
Westinghouse Electric Corporation
Research and Development Center
1310 Beulah Road
Pittsburgh, Pennsylvania 15235

Dr. F. Mansfeld
Rockwell International Science Center
1049 Camino Dos Rios
P.O. Box 1085
Thousand Oaks, California 91360

Professor A. E. Miller
University of Notre Dame
College of Engineering
Notre Dame, Indiana 46556

Dr. Jeff Perkins
Naval Postgraduate School
Monterey, California 93940

Professor H. W. Pickering
Pennsylvania State University
Department of Material Sciences
University Park, Pennsylvania 16802

SUPPLEMENTARY DISTRIBUTION LIST (cont'd)

Dr. William R. Prindle
National Academy of Sciences
National Research Council
2101 Constitution Avenue
Washington, D.C. 20418

Professor R. W. Staehle
Ohio State University
Department of Metallurgical Engineering
Columbus, Ohio 43210

Dr. Barry C. Syrett
Stanford Research Institute
333 Ravenswood Avenue
Menlo Park, California 94025

Dr. R. P. Wei
Lehigh University
Institute for Fracture and
Solid Mechanics
Bethlehem, Pennsylvania 18015

Professor H.G.F. Wilsdorf
University of Virginia
Department of Materials Science
Charlottesville, Virginia 22903

UNCLASSIFIED

SECURITY CLASSIFICATION OF THIS PAGE *(When Data Entered)*

REPORT DOCUMENTATION PAGE		READ INSTRUCTIONS BEFORE COMPLETING FORM
1. REPORT NUMBER	2. GOVT ACCESSION NO.	3. RECIPIENT'S CATALOG NUMBER
4. TITLE *(and Subtitle)* EFFECT OF RARE EARTH ADDITIONS ON STRESS CORROSION CRACKING OF 4340 STEEL.		5. TYPE OF REPORT & PERIOD COVERED TECHNICAL rept. 17 June 1976 - 16 June 1977 6. PERFORMING ORG. REPORT NUMBER ER-7814-3
7. AUTHOR(s) A. A. Sheinker		8. CONTRACT OR GRANT NUMBER(s) N00014-74-C-0365
9. PERFORMING ORGANIZATION NAME AND ADDRESS Materials Technology Laboratory TRW Inc. 23555 Euclid Avenue , Cleveland, Ohio 44117		10. PROGRAM ELEMENT, PROJECT, TASK AREA & WORK UNIT NUMBERS
11. CONTROLLING OFFICE NAME AND ADDRESS Office of Naval Research Department of the Navy 800 North Quincy Street, Arlington Virginia 22217		12. REPORT DATE January 1978 13. NUMBER OF PAGES 44
14. MONITORING AGENCY NAME & ADDRESS *(if different from Controlling Office)*		15. SECURITY CLASS. *(of this report)* Unclassified 15a. DECLASSIFICATION/ DOWNGRADING SCHEDULE

16. DISTRIBUTION STATEMENT *(of this Report)*

Approved for public release, distribution unlimited.

17. DISTRIBUTION STATEMENT *(of the abstract entered in Block 20, if different from Report)*

18. SUPPLEMENTARY NOTES

19. KEY WORDS *(Continue on reverse side if necessary and identify by block number)*

Stress Corrosion Cracking
High Strength Steels
Rare Earth Metals
Hydrogen Embrittlement
Fracture Mechanics
Crack Propagation
Fractography

20. ABSTRACT *(Continue on reverse side if necessary and identify by block number)*

The addition of rare earth elements was investigated as a method of improving the stress corrosion cracking resistance of high strength steels. The addition of cerium at levels of 0.20 and 0.30 weight percent had only a small effect on the stress corrosion cracking resistance of AISI 4340 steel heat treated to a yield strength of approximately 215 ksi (1480 MPa). The stress corrosion cracking threshold (K_{Iscc}) in 3.5 percent sodium chloride solution at room temperature was about the same for the two cerium-bearing steels as it was for 4340 steel without cerium, ranging from 15 to 17 ksi $\sqrt{in.}$ (16.5 to 19 MPa $\sqrt{m}$).

DD FORM 1 JAN 73 1473 EDITION OF 1 NOV 65 IS OBSOLETE
S/N 0102-014-6601 | 405613

UNCLASSIFIED
SECURITY CLASSIFICATION OF THIS PAGE *(When Data Entered)*

20. ABSTSTRACT (continued)

The higher cerium (0.30%) material had longer failure times and lower average crack growth rates than the lower cerium (0.20%) material. The failure times and average crack growth rates for the steel without cerium could not be directly compared with those for the two cerium-bearing steels because of crack branching, which occurred only in the material without cerium. However, it was estimated that, in the absence of branching, the failure times for the non-cerium steel would be shorter and the average crack growth rates higher than those for the lower cerium steel. The cerium additions had no effect on the fractographic morphology of stress corrosion cracking, which was intergranular at low stress intensity levels, with an increasing proportion of dimpled rupture as the stress intensity level increased.